Research Square

Preprints are preliminary reports that have not undergone peer review.
They should not be considered conclusive, used to inform clinical practice,
or referenced by the media as validated information.

Computational Investigations on Viability of Inorganic Cs 2 AgBiI 6 Double Perovskite Semiconductor for Hybrid Solar Cell Modules

Zahid Mahmood
Riphah International University
Muhammad Farooq Nasir
farooq.nasir@riphah.edu.pk

Riphah International University
Irfan Qasim
Rawalpindi Women University
Sikander Azam
University of West Bohemia, New Technologies – Research Centre
Muhammad Imran Malik
National University of Sciences and Technology (NUST)
Asim Rashid
Technical Developer Renewables

Article

Keywords: Density Functional Theory, Double Perovskite, Photovoltaics, Optical Properties, SCAPS-1D

Posted Date: November 9th, 2026

DOI: https://doi.org/10.21203/rs.3.rs-11384793/v1

License: This work is licensed under a Creative Commons Attribution 4.0 International License.
Read Full License

Additional Declarations: No competing interests reported.

Computational Investigations on Viability of Inorganic Cs_2AgBiI_6 Double Perovskite Semiconductor for Hybrid Solar Cell Modules

Zahid Mahmood[1], Muhammad Farooq Nasir[1*], Irfan Qasim[2], Sikander Azam[3], Muhammad Imran Malik[4], Asim Rashid[5]

1 Department of Physics (FEAS), Riphah International University, Islamabad, 44000, Pakistan.
2 Department of Physics, Faculty of Sciences, Rawalpindi Women University, 6th Road, Satellite Town, 46300 Rawalpindi, Pakistan.
3 University of West Bohemia, New Technologies – Research Centre, 8 Univerzitní, Pilsen 306 14, Czech Republic.
4 Department of Humanities and Sciences (DoHS), School of Electrical Engineering and Computer Science (SEECS), National University of Sciences and Technology (NUST), Islamabad, 44000, Pakistan.
5 Technical Developer Renewables, Fortum renewables Oy, POB 100, F1-00048 Keilalahdentie 2-4, Finland.

Corresponding authors:
Muhammad Farooq Nasir
Tel.: +92515469641-7 (ext.260) Cell: +923335157531
*E-mail address: farooq.nasir@riphah.edu.pk

Abstract:

The structural, electronic, and optical properties of lead-free double perovskite Cs_2AgBiI_6 were investigated using density functional theory (DFT) within the generalized gradient approximation (GGA) implemented in Quantum ESPRESSO. Cs_2AgBiI_6 exhibits an indirect band gap, with the valence band maximum and conduction band minimum located at different high-symmetry points. Structural stability was assessed using convex hull analysis and the Goldschmidt tolerance factor, while optical calculations revealed strong visible-light absorption. The obtained material parameters were subsequently employed to design a hybrid solar cell with the configuration Au/Spiro-OMeTAD/Cs_2AgBiI_6/CIGS/CdS/TiO_2/FTO using SCAPS-1D. The optimized device achieved a power conversion efficiency of 44.86%, with an open-circuit voltage of 1.092 V, short-circuit current density of 49.98 mA/cm^2, and fill factor of 82.11%. PVsyst simulations yielded a maximum module power of 1025.9 W at 1000 W/m^2 irradiance, demonstrating the potential of Cs_2AgBiI_6 for efficient lead-free photovoltaics.

Keywords: Density Functional Theory; Double Perovskite; Photovoltaics; Optical Properties; SCAPS-1D.

1. Introduction

Climate change, energy storage, and energy generation have become some of the most discussed challenges in contemporary society. Given the escalating challenges in the energy sector, including the depletion of nonrenewable energy resources and rising CO_2 emissions, the global development of substitute renewable energy technologies has become an urgent necessity. Solar energy, when plentiful, holds the potential to be a reliable resource for future energy demands. Solar cell technology has become a key solution to meet the increasing need for electrical power, driven by the growing demand for high-efficiency photovoltaic modules. In the next two decades, solar-generated electricity could contribute to 20% of global primary energy consumption. As conventional nonrenewable sources diminish, solar energy becomes a crucial solution for power generation. The Sun's energy is abundant and universally accessible, and its growing importance stems from its environmental benefits, as it does not directly contribute to pollution or climate change [1-3]. Over the past 30 years, significant advancements have been made to boost the efficiency of semiconductor solar cells and improve the understanding of their structure. Currently, silicon (Si) is the industry-standard material for photovoltaic cells. Despite continuous efforts to improve device efficiency, the high cost of high-quality silicon required for solar applications remains a barrier to further cost reductions and widespread adoption of the technology.

To overcome these challenges, experts worldwide are exploring various solutions. Recently, the emergence of perovskite-structured materials has opened up opportunities for achieving cost-effective energy production. As a result, there is an ongoing search for alternative, environmentally friendly materials with diverse crystal structures and dimensionalities that can efficiently and reliably be used in solar cells and optoelectronic applications.

Notably, recent advancements in X-ray detectors based on inorganic and organic perovskite $MAPbI_3$ have garnered substantial attention. Ultra-high sensitivity has been demonstrated in $MAPbBr_3$ / $Cs_2AgBiBr_6$ perovskite bulk single crystals and thin films. An additional key benefit of perovskite materials is the ease of fabricating high-quality films. The introduction of perovskite as an active absorber material in solar devices has significantly advanced research on renewable energy materials. Since their first use in PV cells in 2009, the PCE of perovskite-based cells has improved by over 25% in a short period. Moreover, their production costs are notably lower than current technologies, thanks to the abundance of available raw materials [4, 5]. Lead-halide perovskites have gained significant focus due to their high potential in photovoltaics (PVs), photodetectors and light-emitting diodes (LEDs). Over the past years, lead-based metal halide perovskites have revolutionized the photovoltaic field, with PCE increasing from 3.8% at the start in 2009 to 25.7% by 2022. Despite their exceptional performance, the presence of toxic lead (Pb) poses environmental and health risks. Additionally, their lack of chemical

stability remains a major obstacle to commercialization. As a result, research is focused on identifying stable, non-toxic alternatives with diverse crystal structures and dimensionalities for solar cells and optoelectronic applications. Halide double perovskites (HDPs) have gained significant interest in recent years. Almost simultaneously, three separate groups reported the synthesis of bulk Cs_2AgBiX_6 (X= Cl, Br, I) HDPs, which exhibit light absorption in the visible spectrum. However, their direct band gap, which is larger than desired, makes them less suitable for photovoltaic applications using thin films. Consequently, further exploration of alternative materials is warranted. $Cs_2AgInCI_6$, with a direct band gap of approximately 3.3 eV, is limited in its use within the visible region due to this wide band gap. As a result, very few lead-free, all-inorganic HDP materials have been developed for optoelectronic devices [6].

Due to their large or indirect band gaps, these compounds are often unsuitable for high-efficiency photovoltaic applications. Additionally, their reduced mobility compared to $CH_3NH_3PbI_3$ is primarily due to the higher effective mass of charge carriers (e.g., Cs_2AgBiX_6; X= Cl, Br, I). The high density of electron traps and short electron diffusion length in HDPs, such as $Cs_2AgBiBr_6$, are major factors limiting solar cell performance. To address these challenges, several strategies, including alloying with trivalent or monovalent metals, defect engineering, and cation mixing, were employed to modify the energy band gap and improve efficiency. However, much work remains to be done to achieving optimal performance. In recent years, significant attention has been directed towards halide double perovskites (HDPs). Nearly simultaneously, three independent research groups reported the synthesis of bulk Cs_2AgBiI_6 HDPs, which exhibit light absorption in the visible spectrum. However, the band gap of these materials is indirect and slightly larger than ideal for thin-film photovoltaic applications. As a result, researchers are actively exploring alternative solutions. To address lead toxicity and instability in perovskite materials, a direct approach focusing on lead-free, stable replacements is being pursued. One promising candidate for substitution is Sn^{2+}, as it belongs to the same periodic group as Pb and shares similar lone-pair characteristics. These Sn^{2+}-based materials maintain the 3D perovskite structure and exhibit relatively high-power conversion efficiency (PCE). However, the susceptibility of Sn^{2+} to oxidation into Sn^{4+} remains a significant challenge. Furthermore, Sn^{2+}-based compounds, such as SnI_2, may pose health risks due to their strong acidification effects [7, 8].
Recent studies focus on the thorough exploration of the inorganic Cs_2AgBiI_6 material for potential use in optoelectronic devices, particularly solar cells. This material has been designed and integrated for the first time into a novel configuration of solar cell Au/Spiro-OmeTAD/Cs_2AgBiI_6/CIGS/CdS/TiO_2 /FTO. Comprehensive theoretical investigations have been conducted to assess its optical characteristics, including real as well as imaginary parts of the dielectric constant (ε_1, ε_2), refractive index ($n(\omega)$), extinction coefficient

(k(ω)), reflectivity (R(ω)), optical conductivity (σ(ω)) and absorption coefficient (α(ω)). These optical characteristics were used for device simulations, where Cs_2AgBiI_6 was incorporated as the optical absorber. The device's electrical performance was thoroughly analyzed and reported. The outcomes offer valuable insights for design and development of efficient, cost-effective, and ecologically friendly photosensitive devices, contributing to sustainable solutions for energy.

2. Methodology

2.1 Materials Investigations by Quantum Espresso

All theoretical calculations related to density functional theory (DFT) were performed using Quantum ESPRESSO using the plane-wave code to investigate the electronic and optical properties of the novel inorganic double perovskite Cs_2AgBiI_6. To incorporate spin-orbit coupling (SOC) effects, fully relativistic ultra-soft pseudopotentials were employed instead of norm-conserving ones. The generalized gradient approximation (GGA-PBE) functional, established by Perdew, Burke, and Ernzerhof, was utilized as the exchange-correlation functional in this study [9, 10]. This approach maintains a consistent potential across both interstitial and core regions, minimizing discontinuities at the boundaries of the spherical muffin-tin regions. The PBE-sol approximation provided more accurate structural properties than both the GGA and local density approximation (LDA). However, due to the nonappearance of the potential related term in the total Hamiltonian, the accuracy of the electrical characteristics may be slightly compromised To enhance the band gap accuracy, the Tran-Blaha modified Becke-Johnson (TB-mBJ) potential was applied [11, 12].

The energy band structure and density of states of perovskite Cs_2AgBiI_6 were computed using the Quantum espresso package. It was employed to perform a self-consistent calculation scheme in order to retrieve the absorption spectrum and optical excitations. The high frequency real (ω_1) and imaginary (ω_2) components of the dielectric tensor were integrated to compute the optical characteristics using the methods of Gajdos et al. [13] The absorption coefficient (α) was also determined by using the following relation of equation (1),

$$\alpha(\omega) = (\sqrt{2})\,\omega\,[\sqrt{[\sqrt{\varepsilon_1(\omega_2) + \varepsilon_2(\omega_2)}} - \varepsilon_1(\omega)] \quad (1)$$

where ω represents the photon frequency.

The Optical response calculations of the layers (bulk) utilizing the GGA-PBE (HSE-06) functional were investigated using a finer k-points mesh. Polarization is measured by the real dielectric constant, whereas dielectric losses are measured by the imaginary component. Real and imaginary

components together form the dielectric function, which may be expressed in the following equation (2).

$$\varepsilon(\omega) = \varepsilon_1(\omega) + i\varepsilon_2(\omega) \quad (2)$$

The material's structural properties influence optical characteristics such as reflectivity, absorption, loss function, and refractive index. In a cubic material, these properties are isotropic. The reflectivity of any material can be determined using the equation (3) for the dielectric function.

$$R(\omega) = \frac{((\varepsilon_1))1/2-1}{((\varepsilon_1))1/2+1} \quad (3)$$

Reflectivity refers to a material's ability to reflect incident radiation, typically given as percentage of total light that strikes the surface. In the context of extreme ultraviolet (EUV) light, reflectivity peaks arise due to electrical transitions from the maximum of valence band to the lowermost of conduction band. These transitions, where electrons move from a lower energy state to a higher one, are key to understanding how materials interact with high-energy radiation, influencing their optical properties and performance in optoelectronic devices. The double perovskite Cs_2AgBiI_6 under investigation shows promising potential in photocatalysis and photovoltaic applications due to its narrow band gap and ability to absorb significant amounts of UV light [14, 15]. The loss function, which characterizes energy dissipation in the material, can be determined using equation 4. This property makes Cs_2AgBiI_6 a viable candidate for applications involving the conversion of high-energy light into usable electrical energy, enhancing its suitability for energy-related technologies such as solar cells and photocatalytic devices [16-18].

$$L(\omega) = \frac{\varepsilon_2(\omega)}{(\varepsilon_1)2\ (\omega)+(\varepsilon 1)2\ ((\omega)} \quad (4)$$

The loss function plays a key role in identifying two fundamental plasmonic processes: energy dissipation and electron excitation. It describes how a material absorbs and loses energy when interacting with electromagnetic radiation, such as light. In plasmonics, this process occurs when incident light excites free electrons, causing them to oscillate and generate surface plasmons. The loss function measures the energy that is absorbed or dissipated, rather than reflected, offering valuable insights into the material's effectiveness in plasmonic applications, including sensors and energy harvesting technologies [19-21]. The refractive index is calculated to determine how light propagates through a material, influencing its optical characteristics. It plays a critical role in optoelectronic devices by affecting light absorption, reflection, and transmission, thus impacting the efficiency and performance of devices like solar cells. The refractive index was calculated using Equation (5).

$$n(\omega) = \frac{\sqrt{2}}{2}[\varepsilon 1 + \sqrt{\varepsilon 1^2 + \varepsilon 2^2}] \quad (5)$$

When atoms are covalently bonded and photons interact with the material, the refractive index becomes crucial. The refractive index increases with the expansion of the electronic cloud and the increase in density of Cs_2AgBiI_6. The absorption coefficient is directly related to the imaginary part of the dielectric function and the optical transmission. For Cs_2AgBiI_6, the calculated refractive index and extinction coefficient describe the optical response of Cs_2AgBiI_6 over the investigated photon-energy range. This material is suitable as an absorber due to its band gap range of 1 to 2.25 eV and strong absorption capabilities.

2.2 Solar Cell Investigations by SCAPS-1D

SCAPS-1D, the Solar Cell Capacitance Simulator, was technically developed by Mark Burgelman and team members at the University of Ghent to facilitate the theoretical analysis of solar cells. PVSyst is used for photovoltaic system and module-level performance analysis based on electrical, optical, thermal, meteorological, and system-design parameters. It offers valuable insights into the output performance of PV cells, helping to optimize their design and functionality by modeling key mechanisms involved in energy conversion. The Poisson equation provides the link between the charge density distribution and the electrostatic potential [22-24].

$$\frac{d}{dx}\left(\varepsilon(x)\frac{d\psi}{dx}\right) = -q\left[p(x) - n(x) + N_D^+(x) - N_A^-(x) + \rho_{trap}(x)\right] \quad (6)$$

Where ψ = electrostatic potential, ε(x) = absolute permittivity, q = elementary charge, n(x) and p(x) are the free hole and electron concentration, $N_D^+(x)$ **and**, $N_A^-(x)$ denote the ionized donor and acceptor impurity densities, $\rho_{trap}(x)$ trap charge density, The continuity equations for holes and electrons are given by:

$$\frac{\partial \mathrm{p}}{\partial \mathrm{t}} = \frac{1}{q}\frac{\partial J_n}{\partial x} + \mathrm{U_n} \quad (7)$$

$$\frac{\partial p}{\partial t} = -\frac{1}{q}\frac{\partial Jp}{\partial x} + \mathrm{U_p} \quad (8)$$

Where, J_n=current densities of electrons, J_p=current densities of holes, R_p = Recombination rate for holes, U_n and U_p are Net recombination rates for electrons and holes, The electron and hole current densities are calculated using the drift-diffusion equations for charge carriers.

$$J_n = q\mu_n nE + qD_n\frac{dn}{dx} = -q\mu_n n\frac{d\psi}{dx} + qD_n\frac{dn}{dx} \quad (9)$$

$$J_p = q\mu_p pE - qD_p\frac{dp}{dx} = -q\mu_p p\frac{d\psi}{dx} - qD_p\frac{dp}{dx} \quad (10)$$

Where μ_n is electron mobility, μ_p the hole holes mobility, D_n and D_p are electron and hole diffusion coefficients, The fill factor (FF) can be determined using Equation

$$\mathrm{FF} = \frac{\mathrm{Jmp}\ X\ Vmp}{J_{sc}\ X\ Voc} \quad (11)$$

Efficiency is measured by the relation,

$$\eta = \frac{V_{oc}\ \mathrm{X}\ J_{sc}\ \mathrm{X}\ \mathrm{FF}}{Pin} \quad (12)$$

The input parameters obtained through DFT are incorporated in SCAPS 1D simulation package to determine the n-i-p planar PSC performance for the device configuration Au/Spiro-OmeTAD/Cs_2AgBiI_6/CIGS/CdS/TiO_2/FTO. The SCAPS-1D simulation package enables the calculation of essential solar cell parameters, including short-circuit current density (J_{sc}), open-circuit voltage (V_{oc}, fill factor (FF), and power conversion efficiency (PCE). over varying thicknesses and temperatures [25-27]. This simulation tool is versatile, capable of operating under both illuminated and dark conditions, and incorporates the effects of diverse temperature environments. It provides a comprehensive analysis of solar cell performance, enabling the evaluation of device characteristics under a wide range of operating conditions.

2.3 Solar Module Investigations by PVSyst

The optimized performance data from the single solar cell were provided as input to the PVSyst software for module analysis and simulations. PVSyst is used for photovoltaic system and module-level performance analysis based on electrical, optical, thermal, meteorological, and system-design parameters.It is commonly used as a tool for simulating, designing and assessing the performance of PV systems. By incorporating system configuration, local weather data, and module specifications, PVSyst generates a model to simulate energy output [28-30]. This model allows the estimation of yearly energy production, system efficiency, and capacity factor. It also considers features such as shading, inverter efficiency and systematic losses, providing a convincing performance evaluation. Furthermore, PVSyst includes an extensive meteorological database for over 30,000 locations globally, allowing accurate simulations under varying conditions of weather. The software also provides thorough financial analysis, cost evaluations, payback time, and investment returns, aiding in assessment of the cost-effectiveness of solar PV systems. PVSyst is an effective tool for improving the design and output of PV systems [31-33].

3. Results and Discussion

3.1 Structural properties

The crystal structure of Cs_2AgBiI_6 is an ordered double perovskite with a characteristic arrangement of Cs, Ag, Bi, and I atoms within the unit cell, as shown in Figure 1. The optimized structure crystallizes in the cubic Fm-3m space group (No. 225), which is the typical crystal structure reported for Cs_2AgBiI_6. This is consistent with the optimized lattice parameters, where a = b = c = 12.25372 Å, confirming the cubic geometry. The unit cell volume is calculated to be 1839.94 $Å^3$. The Cs_2AgBiI_6 structure is composed of cesium (Cs), silver (Ag), bismuth (Bi), and iodine (I) atoms. The Cs atoms occupy various positions within the unit cell, contributing to the material's stability. Specifically, there are eight Cs atoms located at specific fractional coordinates

(e.g., 0.25000, 0.25000, 0.75000), ensuring the formation of a stable perovskite structure. These positions reflect a repeating pattern that helps form the backbone of the material. In addition to Cs, silver (Ag) and bismuth (Bi) atoms are positioned symmetrically within the unit cell, with each metal ion placed at fractional coordinates that repeat in the lattice. Silver ions, in particular, play an important role in the electrical characteristics of the material, while bismuth ions contribute to its optical and electronic behavior. Finally, iodine atoms are arranged in a way that forms an essential part of the halide framework, binding the metal ions together and influencing the material's conductivity.

The structure of Cs_2AgBiI_6 is significant for its potential in photovoltaic and optoelectronic applications, as its unique arrangement allows for efficient charge transport and light absorption, essential features for solar cell materials. The analysis of Goldschmidt's tolerance factor (τ) and the octahedral factor involves the application of specific equations to evaluate the stability and structure of perovskite materials. The tolerance factor (τ) helps assess how well the ionic radii of the constituent elements fit together in the crystal lattice, which is crucial for understanding the formation of stable perovskite structures. The formula for the tolerance factor is:

$$\tau = \frac{R_A + R_X}{\sqrt{2}\,(R_B + R_X)} \tag{13}$$

where the ionic radii R_A, R_B and R_X denote the A-site cation, B-site cation, and anion respectively. A value of (τ) close to 1 typically indicates a stable perovskite structure.

The octahedral factor, on the other hand, provides insight into the ability of the B-site cation to form an octahedral coordination with the surrounding anions. The octahedral factor (μ) may be calculated using the ratio of the ionic radii of B-site cation and anion:

$$\mu = \frac{R_B}{R_X} \tag{14}$$

This factor helps determine the structural properties of the material, including its ability to form octahedra, which is fundamental in perovskite crystal formation. Both factors are essential in predicting the crystallization behavior and stability of materials used in various applications, including photovoltaic and optoelectronic devices.

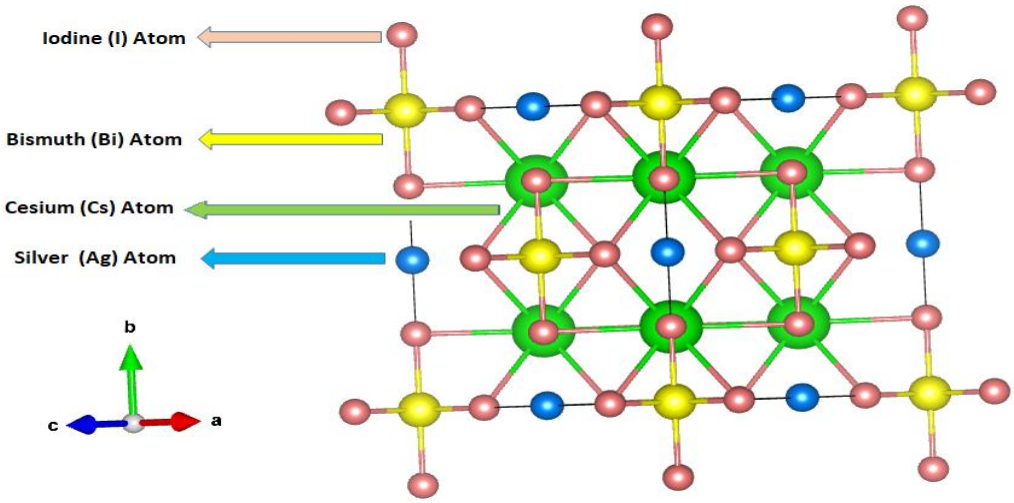


Figure-1. Structure of Cs_2AgBiI_6 with atomic position.

3.2 Electronic properties

Calculating the electronic properties using DFT is crucial for understanding the behavior and performance in various applications, such as semiconductors, photovoltaics, and sensors. DFT provides a thorough description of the material's electronic structure, enabling the calculation of key properties like the density of states (DOS), partial DOS, energy gap (E_g) and total DOS. The DOS discloses the layout of electronic states at different energies, while the PDOS further gives contributions from precise atoms or orbitals, offering insights into the material's chemical bonding and electronic interactions. The energy band diagram provides essential information on the material's conduction and valence bands, helping to predict electrical conductivity, band gap, and other key characteristics. These calculations are vital for designing and optimizing materials with tailored electronic properties, facilitating advancements in electronics, energy storage, and renewable energy technologies.

3.2.1 Energy Band

The electronic band structure of a material offers critical insights into its energy band gap (Eg) and the nature of the energy gap, whether direct or indirect. This information is essential for determining the material's electronic properties and potential applications. Additionally, the band structure helps classify materials into semiconductors, metals, or insulators, based on the distribution of energy levels. For the double perovskite Cs_2AgBiI_6, the computed electronic band structure is shown in Figure 2, highlighting the highly symmetric directions within the first Brillouin zone (BZ). These calculations were performed using the GGA+U method, employing a high-

symmetry track Γ–X–W–K–L–W, as illustrated in Figure 2. This analysis provides useful information about the electronic characteristics of the material , which are critical for evaluating its suitability for applications such as optoelectronics and photovoltaics. The estimation of the band gap using the exchange-correlation functional PBE often underestimates the actual value. To enhance accuracy in band gap determination, the Hubbard-U correction was incorporated. The studied compounds exhibit band gap values within the ideal range for solar cell applications, typically between 0.6 and 1.7 eV. Figure 2 depicts the estimated energy band gap of the material, revealing an indirect band gap of 1.404 eV. This optimal band gap suggests that the material may offer higher efficiency, faster switching capabilities, operation at elevated temperatures, and a more compact form factor. The band structure analysis of Cs_2AgBiI_6 highlights its potential for applications in photovoltaics.

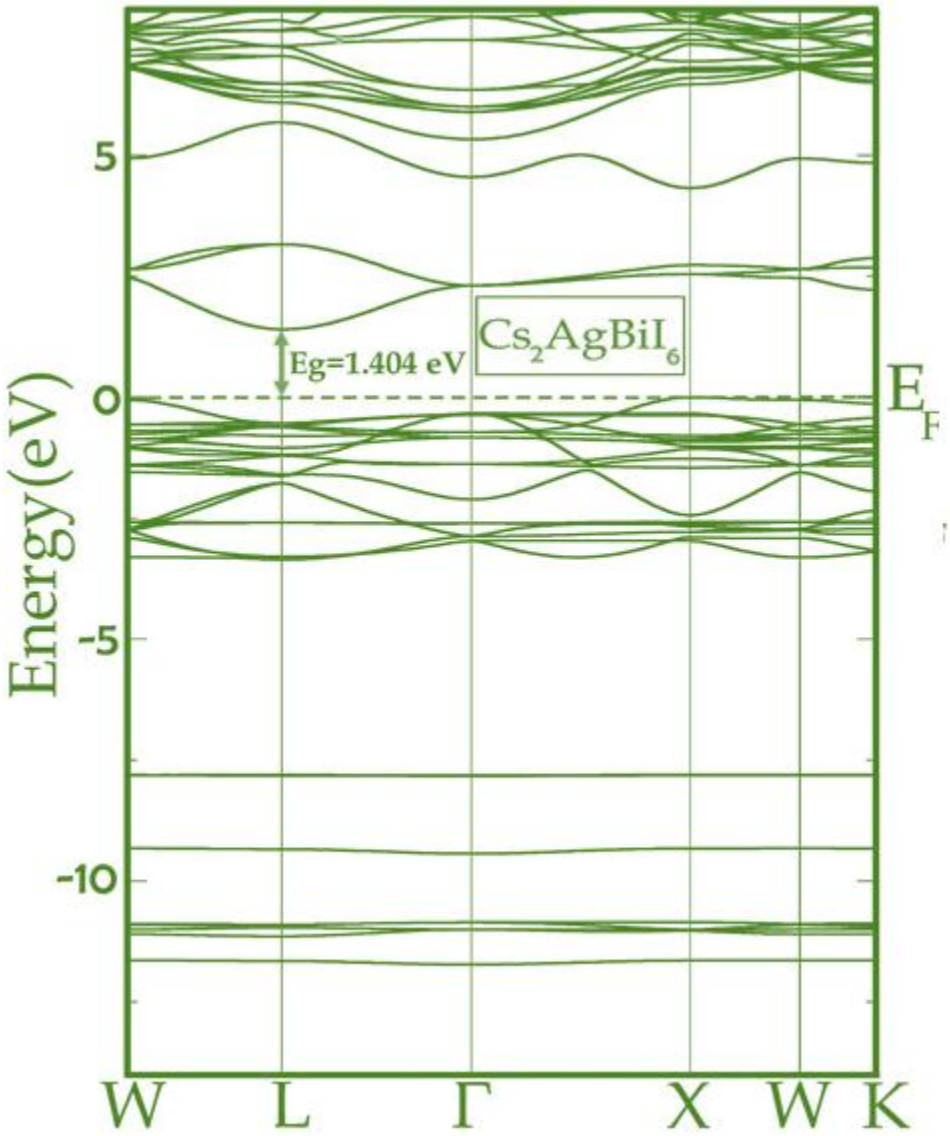


Figure-2. Energy band structure of double perovskite Cs_2AgBiI_6 material.

3.2.2 Density of States

The DOS shows the number of electronic states per unit volume per unit energy, providing critical insights into the electronic structure of the material. For a comprehensive understanding of the material's properties, both TDOS and PDOS were calculated. Both offer detailed information about the elemental and orbital contributions to the electronic structure. Specifically, DOS quantifies the density of electronic states, inversely related to the first derivative of E(k) in context of wave vector k, while the effective mass is proportional to the curvature of E(k). The PDOS illustrates elemental and orbital contributions of electrons within the solid.In the current analysis of the elpasolite Cs_2AgBiI_6, the TDOS and PDOS highlight the total, element-specific, and orbital-specific contributions. The results indicate that Cs-s, Bi-d, and I-p orbitals significantly contribute to the valence band, located below the Fermi level (set to 0 for convenience). In contrast, orbitals in the conduction band play an active role above the Fermi level. The band structure and DOS of Cs_2AgBiI_6 were calculated using both the GGA and mBJ potentials. The calculated band gap depends on the electronic-structure method employed. The band gap obtained using the standard GGA potential is 2.04eV, while the inclusion of the more advanced mBJ potential yields a corrected band gap of 1.12eV (with the optimized band structure configuration yielding 1.404eV, as depicted in Figure 3). The difference between the calculated values is attributed to the choice of exchange-correlation functional and the inclusion of spin–orbit coupling effects. The band gap used in the SCAPS-1D simulation was set according to the optimized mBJ result of 1.404eV to ensure accurate device modeling and consistency with the optical properties

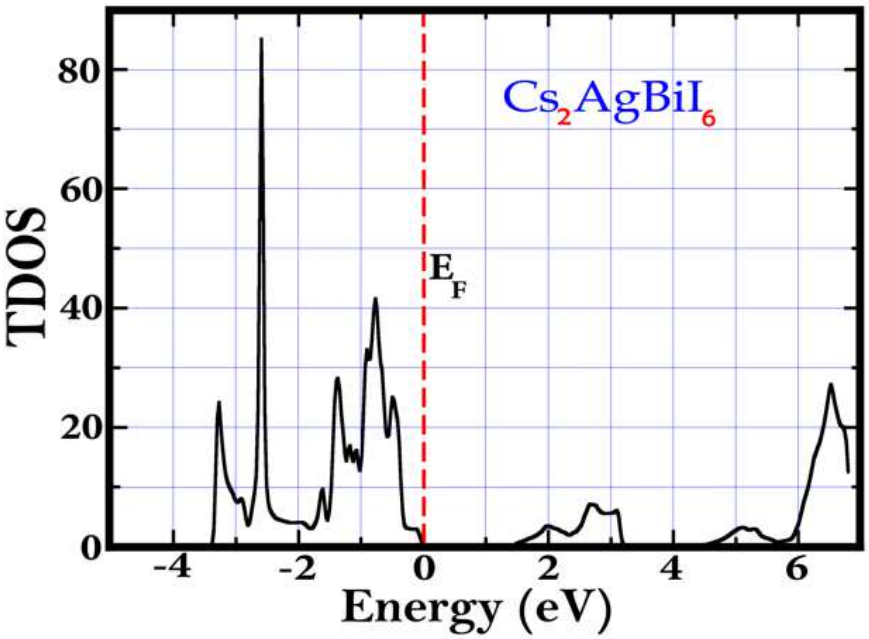


Figure-3. TDOS of the double perovskite material Cs_2AgBiI_6.

Employing the modified Becke–Johnson (mBJ) potential for Cs_2AgBiI_6, it was observed that the transition between the valence band (VB) and the conduction band (CB) is indirect [34]. Among the methods compared, the TB-mBJ potential proved to be highly effective in determining the material's band gap, with results closely aligning with experimental data.

In this study, a detailed analysis of TDOS and PDOS has been conducted to investigate the contributions of specific atoms and orbitals to the electronic structure of Cs_2AgBiI_6. The TDOS and PDOS analyses, performed using the mBJ potential, provide insights into the contributions of elements in the VB and CB. Figure 3 illustrates the TDOS within the energy range of -4 eV to 6 eV. The band gap observed in the TDOS corresponds well with the band structure diagram. The results indicate that Cs_2AgBiI_6 exhibits significant contributions in the VB, while contributions in the CB near the Fermi level are relatively minor. This analysis highlights the material's potential for optoelectronic applications.

The elemental density of states (EDOS) analysis for Cs_2AgBiI_6 highlights the dominant role of Ag, Bi, and I orbitals in shaping the valence band as shown in the figure 4. Ag-d, Bi-p, and I-p orbitals exhibit significant overlap, contributing extensively to the states near the Fermi level. This overlap facilitates effective charge carrier mobility, which is crucial for the material's optoelectronic performance. The pronounced involvement of these orbitals in the valence band underscores their contribution to the material's band structure and energy alignment, making Cs_2AgBiI_6 a promising candidate for photovoltaic and other semiconductor-based applications.

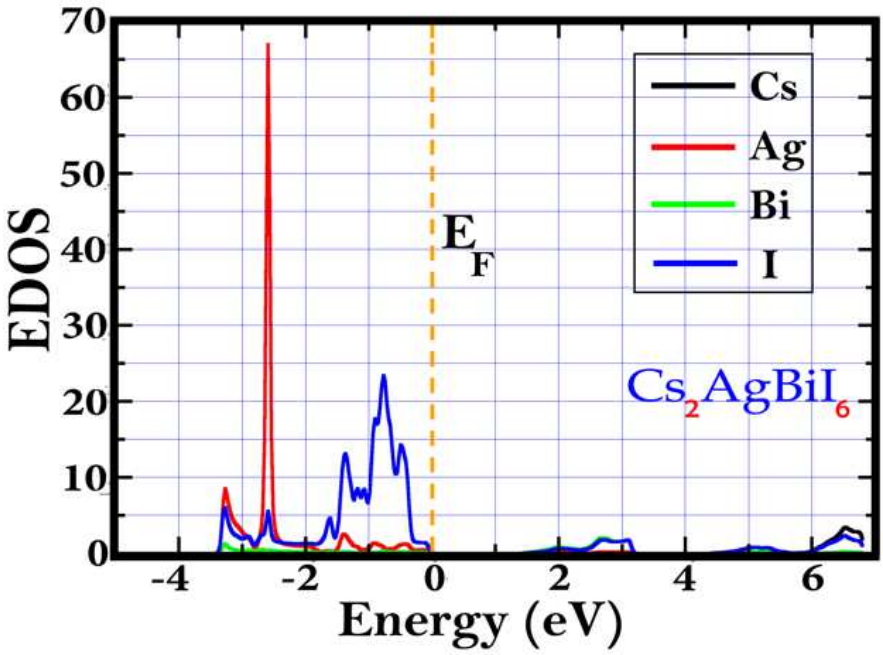


Figure-4. Elemental density of states (EDOS) of the solar perovskite material Cs_2AgBiI_6.

3.3 Optical properties

The optical properties of materials play an important role in various optoelectronics and PV applications. The optical properties of materials can be analyzed through parameters such as the dielectric function, absorption coefficient ($\alpha(\omega)$), reflectivity ($R(\omega)$), conductivity ($\sigma(\omega)$), optical loss function ($L(\omega)$), extinction coefficient ($K(\omega)$) and the refractive index ($n(\omega)$). These parameters are critical for understanding the material's capacity to absorb visible light energy and its electrical polarization characteristics. By calculating these properties, insights into the material's optical behavior are obtained. Results suggest that UV photons transmit more effectively through the material compared to those in the IR or visible spectra. Within the visible range, the optical behavior aligns with typical metallic characteristics, governed by the dielectric function.

The behavior of the real part of the dielectric constant ($\varepsilon_1(\omega)$) versus energy provides critical insights into the material's optical response as shown in Figure 5(a) for Cs_2AgBiI_6 material. The first peak, reaching a value of 9 at 2.1 eV, corresponds to the material's strong polarization response to incident photons at lower energies, signifying electronic transitions near the band edge. The decrease after this peak indicates reduced electronic polarizability as energy increases. The second peak at 6.9 eV, reaching 4.1, suggests another significant electronic transition, likely involving higher-energy states. This peak is indicative of inter-band transitions, where electrons move between deeper valence bands and conduction bands.

The gradual decrease in $\varepsilon_1(\omega)$ beyond this point reflects diminished electronic polarization due to fewer available states at higher energies. The overall trend

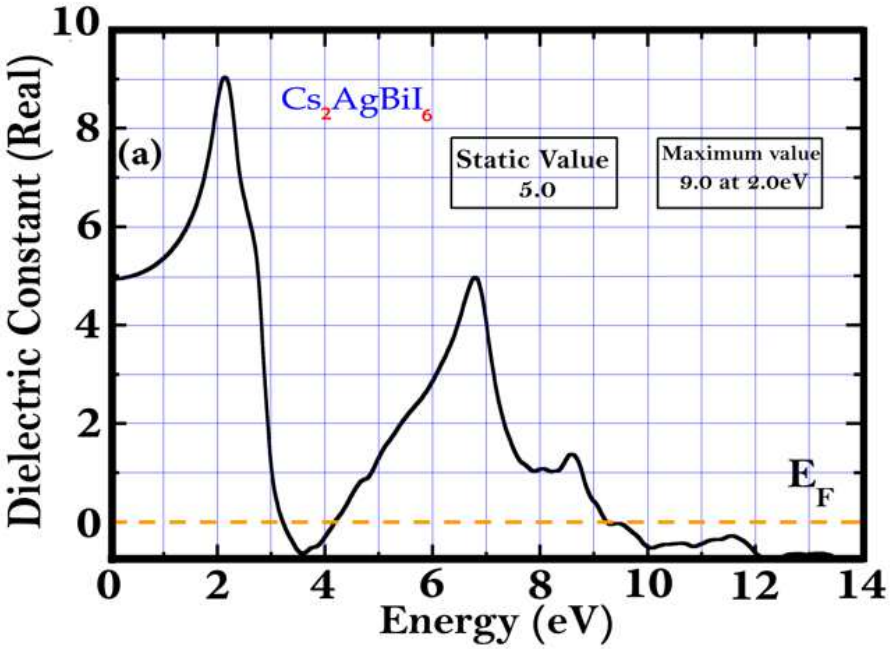
demonstrates how $\varepsilon_1(\omega)$ relates to the material's optical dispersion, with higher values enhancing the refractive index and light-matter interaction, essential for optical applications like photovoltaics or sensors. The overall dielectric constant is obtained by the equation given below;

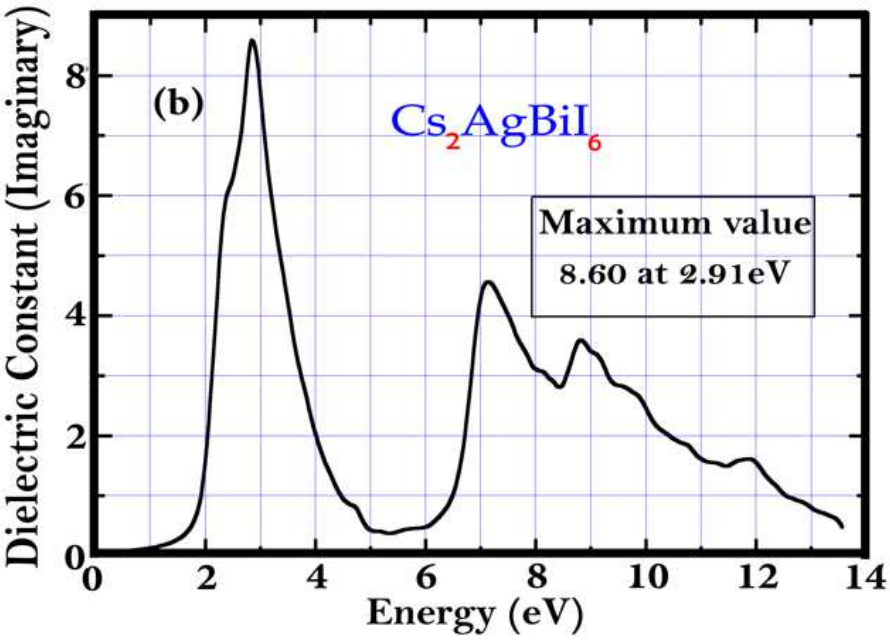
$$\varepsilon(\omega) = \varepsilon_1(\omega) + i\varepsilon_2(\omega) \quad (15)$$

Where $\varepsilon_1(\omega)$ represent the real component and $\varepsilon_2(\omega)$ represent the imaginary component of the dielectric function. The imaginary part (ε_2 (ω)) of dielectric constant provides critical insights into the material's optical absorption properties, as it is directly associated with the inter-band electronic transitions as shown in the figure 5(b). The sharp peak at 2.9 eV, reaching a value of 8.9, indicates a strong absorption due to significant electronic transitions between the valence and conduction band. This energy corresponds to a critical point in the electronic band structure where the density of available electronic states is high, leading to enhanced optical absorption. Following this peak, the rapid decrease in $\varepsilon_2(\omega)$ reflects reduced absorption as fewer transitions occur at higher energy levels. The second peak at 6.1 eV, with a value of 4.5, indicates another set of electronic transitions involving deeper valence states and higher conduction states. Beyond this, the gradual decrease with "kink-like" features suggests minor contributions from higher-energy transitions, which gradually diminish as the photon energy increases. These peaks and features highlight the photon energy ranges where the material exhibits significant optical activity, providing a fingerprint of its electronic structure. Peaks in $\varepsilon_2(\omega)$ identify energy levels where strong inter-band transitions occur, critical for understanding material performance in optoelectronic devices, photovoltaics, and light-absorbing applications. This behavior underlines the material's suitability for energy conversion technologies.

The absorption versus energy plot of Cs_2AgBiI_6 illustrates the material's ability to absorb photons at various energy levels as given in figure 5 (c). The first peak at 2.9 eV, corresponding to an absorption of 50, suggests a strong electronic transition, likely from the valence band to the conduction band, where available states facilitate photon absorption. This initial rise is followed by a slight decrease, indicating reduced absorption as photon energy increases beyond the first critical transition.

The subsequent rise and peak at 6.4 eV, with an absorption of 76, corresponds to a second prominent transition, possibly involving higher energy electronic states. The peak at 10 eV with an absorption of 125 indicates even more pronounced electronic transitions, involving deeper levels or higher conduction states. Afterward, the kink-like behavior reflects a gradual decrease in absorption, showing diminished contribution from higher-energy transitions. Finally, the maximum absorption at 12.1 eV and 131 absorption units signifies a strong absorption feature, potentially linked to excitonic or inter-band transitions at this energy. This behavior highlights the material's efficiency in absorbing light across different photon energies, reflecting its potential for optoelectronic applications, particularly in solar cells.


(a)
Cs2AgBiI6
Static Value
5.0
Maximum value
9.0 at 2.0eV
E_F
Dielectric Constant (Real)
Energy (eV)
0
2
4
6
8
10
12
14


(b)
Cs2AgBiI6
Maximum value
8.60 at 2.91eV
Dielectric Constant (Imaginary)
Energy (eV)
0
2
4
6
8
10
12
14

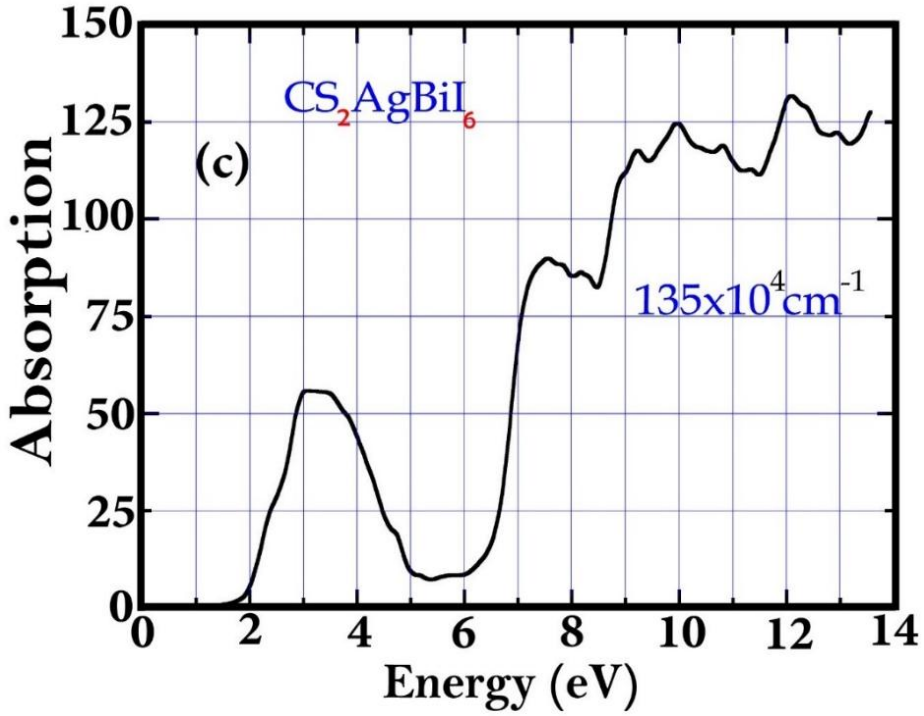


Figure-5. (a) The real part $\varepsilon_1(\omega)$ of dielectric constant of Cs_2AgBI_6 by using mBj potential, (b) The imaginary part $\varepsilon_2(\omega)$ of dielectric constant of Cs_2AgBI_6 by using mBj potential. (c) Absorption coefficient of the Cs_2AgBI_6 by using mBj potential.

Reflectivity serves as a metric for determining the portion of light that a material reflects at a specific angle of incidence, the degree of reflectivity exhibited by a material can be tailored by manipulating its surface properties, thereby altering its optical characteristics to suit specific optoelectronic applications. Across all the materials under study, the highest reflectivity is observed under visible and near UV region. The photon-energy-depended graph illustrating reflectivity is presented in figure 6. Reflectivity is a key measure, revealing how light interacts with a surface. It holds significance in various fields, from optics to materials science, enabling detailed analysis and scientific progress. The presence of absorption peaks within the visible spectrum indicates the favorable performance of the investigated substance in this range. A thorough investigation of their optical properties reveals significant photoelectric characteristics, suggesting a potential for the utilization in the absorber layer of solar cells. As the energy level increases, there is a corresponding rise in reflectivity. It is imperative to maintain a consistent energy level of 14 eV for materials. However, it is noteworthy that once the desired energy level is attained, the reflectivity behavior changes.

In the compound Cs_2AgBiI_6. An intraband transition is observed Additionally, weak peaks in the UV range indicate inter-band transitions. Notably, as the energy band gap widens, the material's reflectance decreases. Conversely, as the halogen size increases, so does the value of R. This rise in R is attributed to the large size and consequently larger number of electrons

in B and Cl. Moreover, this increase may also be due to the absorption edge shifting to lower energies, resulting in more incident radiation being reflected. The remarkable reflectivity values in the visible region (between 1.4 to 4.0 eV) of these compounds underscore their potential for application in optoelectronic devices.

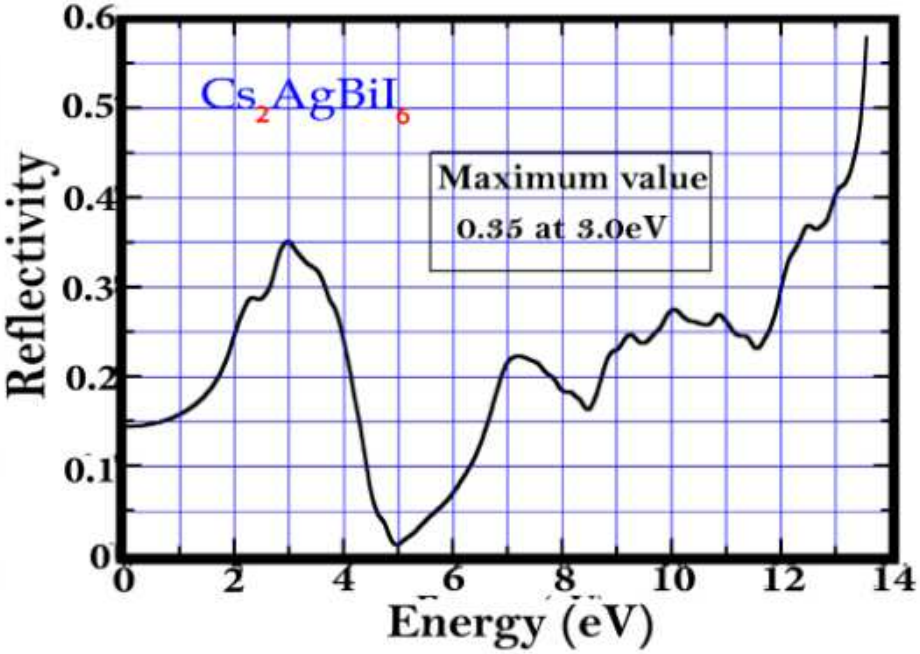


Figure-6. The reflectivity R(ω) of Cs_2AgBI_6 by using mBj potential.

In optics, the refractive index characterizes how light behaves within a material. Figure 7 represents the refractive index of the material under consideration. When light travels through different materials, it does so at varying speed, causing the refractive index of the material to change accordingly. The refractive index and optical reflectivity spectra of Cs_2AgBiI_6 are calculated from the dielectric function using the mBJ method. The results are shown in figure 7.

$$n(\omega) = \sqrt{\frac{\varepsilon_1(\omega)}{\varepsilon_o}} \qquad (16)$$

From initial observation, it is apparent that both spectra of $\varepsilon_1(\omega)$ and $n(\omega)$ exhibit similarities. Additionally, the analyzed results in figure 7 show that the refractive index n (ω) increases with energy, displaying a prominent peak at 3.0 eV for the Cs_2AgBiI_6 material. Subsequent peaks are observed at 7.0 eV and

8.34 eV, which are also attributed to the Cs_2AgBiI_6 compound.

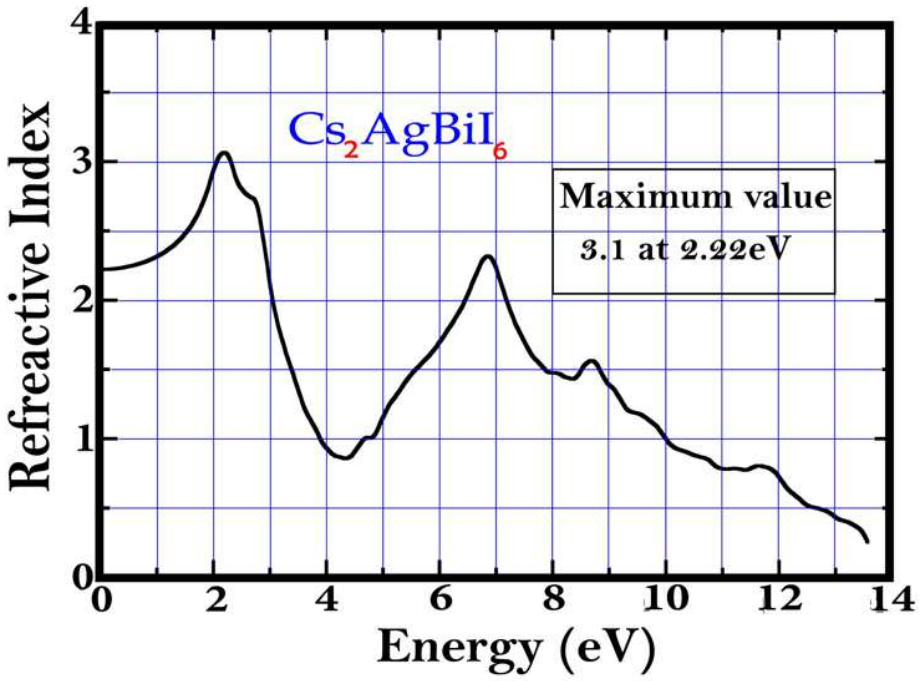


Figure-7. The refractive index of Cs_2AgBiI_6 by using mBj potential.

The energy loss versus energy plot of Cs_2AgBiI_6 provides insight into the material's optical response, particularly how it absorbs and dissipates energy at various photon energies as shown in figure 8. The first major peak at 4.25 eV, with a maximum value of 8.25 on the vertical axis, indicates a significant interaction between the material and incoming photons, where the material absorbs energy efficiently. This peak corresponds to an intense absorption region, suggesting that at this energy, the material undergoes strong electronic transitions or excitations. The sharp decrease after the first peak suggests a reduction in energy loss, meaning that fewer photon interactions occur within this range, and the material absorbs less energy. As the energy increases further, the plot exhibits a gradual increase in energy loss, indicating that the material begins to absorb energy again, but with diminishing efficiency. The peaks at 11.5 eV and 13.1 eV, corresponding to lower energy loss values (0.64 and 0.77, respectively), show the material's response to higher-energy photons, which might correspond to higher energy excitations or transitions. The overall trend reveals that the material becomes more responsive to high-energy photons, indicating the presence of higher energy absorption states or resonance phenomena in these energy ranges, which are critical for optoelectronics.

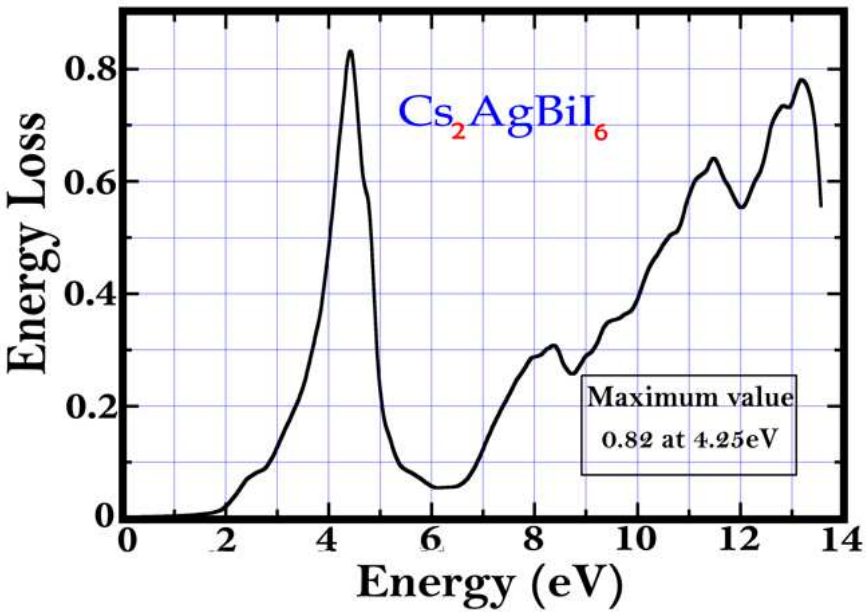


Figure-8. The Energy loss function of dielectric constant of Cs_2AgBI_6 by using mBj potential.

The optical conductivity versus energy plot in figure 9 reveals how a material conducts electricity in response to optical excitation, indicating electronic transitions, absorption efficiency, and interaction with light. The optical conductivity versus energy plot provides insights into the material's electronic transitions and its ability to respond to light at various energy levels. The plot starts at zero, indicating no optical conductivity at lower energies, as no electronic transitions occur. The first peak at 2.9 eV corresponds to an initial increase in optical conductivity, suggesting the onset of electronic excitations or transitions from the valence to conduction band. Following this the peaks in the optical conductivity spectrum indicate energy regions with enhanced optical transitions. Their detailed assignment requires analysis of the electronic band structure and the corresponding interband transition contributions. At 7.23 eV, a second peak emerges, corresponding to another transition, which likely reflects a shift in the material's electronic structure or the onset of higher energy excitations. The peak at 8.9 eV could represent another transition, followed by a "kinky" gradual decrease, signifying a complex relationship between energy and optical conductivity as the material's electronic states reach saturation or diminishing interaction with incident light.

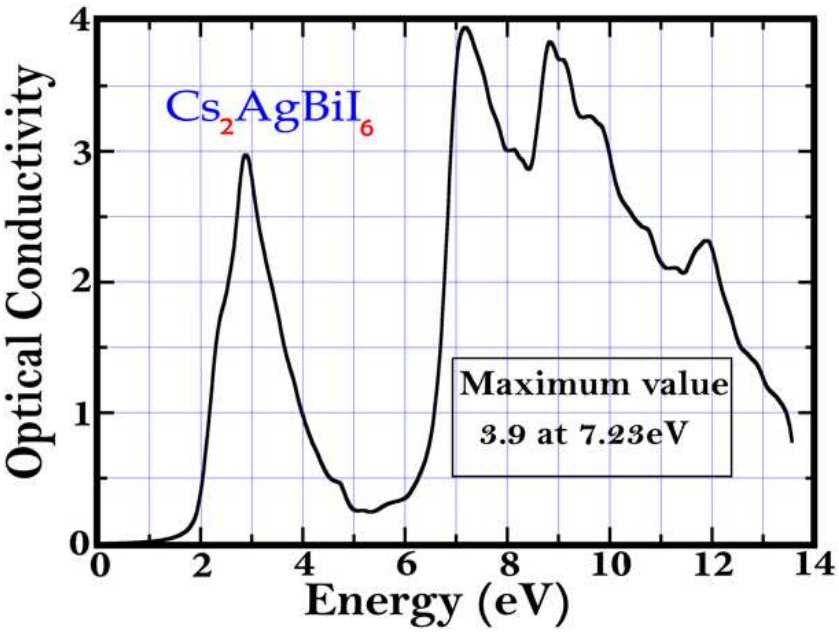


Figure-9. The Optical conductivity of dielectric constant of Cs_2AgBiI_6 by using mBj potential

4. Solar Cell Design.

A novel photovoltaic device configuration shown in figure 10, Au/Spiro-OMeTAD/Cs_2AgBiI_6/CIGS/CdS/TiO_2/FTO, is proposed to achieve superior optoelectronic performance and optimized charge carrier dynamics.

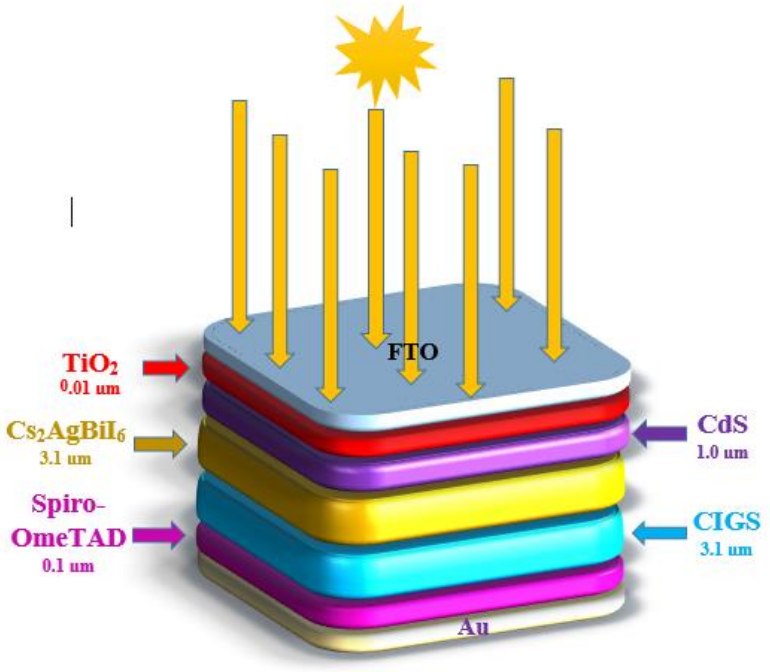


Figure-10. Solar cell structure.

Each functional layer within this architecture is carefully selected to enhance light absorption, minimize recombination losses, and facilitate efficient charge transport. The FTO (Fluorine-doped Tin Oxide) layer is utilized as a transparent conducting electrode, allowing efficient photon penetration and charge collection. TiO_2, employed as the electron transport layer (ETL), ensures selective electron extraction and prevents carrier recombination at the interface. The CdS buffer layer effectively reduces energy barrier mismatches between the absorber and ETL, facilitating charge transfer while mitigating interface defects. The CIGS layer was included as a secondary absorber in the proposed multilayer architecture. Its contribution to the device performance was evaluated through the SCAPS-1D simulation. The Cs_2AgBiI_6 perovskite layer, serving as the primary light-harvesting material, exhibits a suitable band gap, strong optical absorption, and excellent environmental stability. Spiro-OMeTAD, functioning as the hole transport layer (HTL), ensures efficient hole extraction and transportation toward the metal back contact, thereby minimizing recombination losses. The gold (Au) back electrode provides high electrical conductivity, ensuring efficient charge collection and stability.

The energy band alignment of these layers, depicted in figure 11, demonstrates optimal conduction and valence band offsets that facilitate charge carrier separation and transport while suppressing interfacial recombination. To ensure precise simulation and performance evaluation, The material parameters used in the SCAPS-1D simulations were obtained from available DFT calculations and published literature. Parameters not directly available from first-principles calculations were adopted from reported values or defined as simulation inputs, as presented in Table-1. This optimized multi-layered architecture holds significant potential for achieving high photovoltaic efficiency with improved thermal and environmental stability.

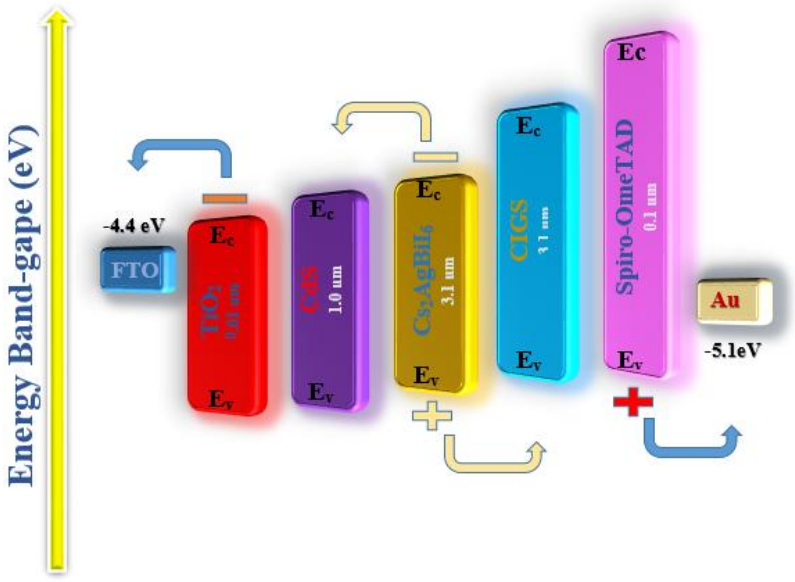


Figure-11. Energy band diagram of solar cell.

Table 1. Material parameters of Tio_2 (ETL) layer, Cs_2AgBiI_6 (absorber layer) , CIGS (absorber layer), Spiro-OmeTAD (HTL) layer and CdS (buffer layer).

Materials parameters	Spiro-OmeTAD	CIGS layer	Cs_2AgBiI_6 layer	Tio_2 layer	CdS
Thickness (μm)	0.1 (optimized)	3.1 (optimized)	3.1 (optimized)	0.01(optimized)	1.0(optimized)
Energy band-gap (eV)	3.17	1.50	1.404	3.20	2.44
Electron Affinity	2.05	4.40	3.9	4.0	4.40
Dielectric Permittivity	3.0	13.60	6.5	10.00	10.00
CB DOS	2.20E+18	2.20E+18	1.0E+19	1.00E+21	2.2E+18
VB DOS	1.80E+19	1.90E+19	1.0E+19	2.00E+20	1.8E+19
Electron/hole thermal velocity	1.00E+7	1.00E+7	1.0E+7	1.00E+7	1.00E+7
Electron Mobility	2.00E-4	1.00E+2	2.0E+0	2.0E+1	1.00E+2
Hole Mobility	2.00E-4	2.50E+1	2.0E+0	1.0E+1	2.50E+1
N_d	0	0	0	5.0E+19	1.00E+18
N_a	4100E+19	1.00E+18	1.00E+15	0	0

5. Solar Cell Characteristics

The current-voltage (J-V) characteristics shown in Figure 12 provide valuable insights of the proposed Au/Spiro-OmeTAD/Cs_2AgBiI_6/CIGS/CdS/TiO_2 solar cell. Current density (J_{sc}) values on the vertical axis indicate the direction of current flow from device to the system. Electrical parameters J_{sc}, V_{oc}, FF, and PCE show output performance of Cs_2AgBiI_6-based solar cell. Adjustments to the thicknesses of the structural layers play a significant role in achieving optimized results. The charge carrier generation is directly dependent on the absorption of photon energy, which is optimized through layer thickness adjustments. In the proposed Cs_2AgBiI_6-based perovskite solar cell, an inorganic absorber is used, and its output performance depends on incident photon energy and its absorption properties. This relationship is governed by E_g of the material. Photons with energies greater than the band gap can promote electrons from the valence band to the conduction band, contributing to photocarrier generation. Photons with energies below the fundamental band gap generally cannot undergo ordinary band-to-band absorption in an ideal semiconductor.

In the context of solar cells, photons with energies greater than the band gap energy of the absorber material are typically absorbed in ultraviolet (UV), visible and infrared (IR) regions, which corresponds to the basic principle of harnessing solar energy. The highest irradiation intensities lie in this region, which can effectively serve the purpose. The composition showed a remarkable power conversion efficiency of 44.86% along with open-circuit voltage (V_{oc}) of 1.092 V, short circuit current density (J_{sc}) of 49.98mA/cm^2 and a healthy fill factor of 82.11%.

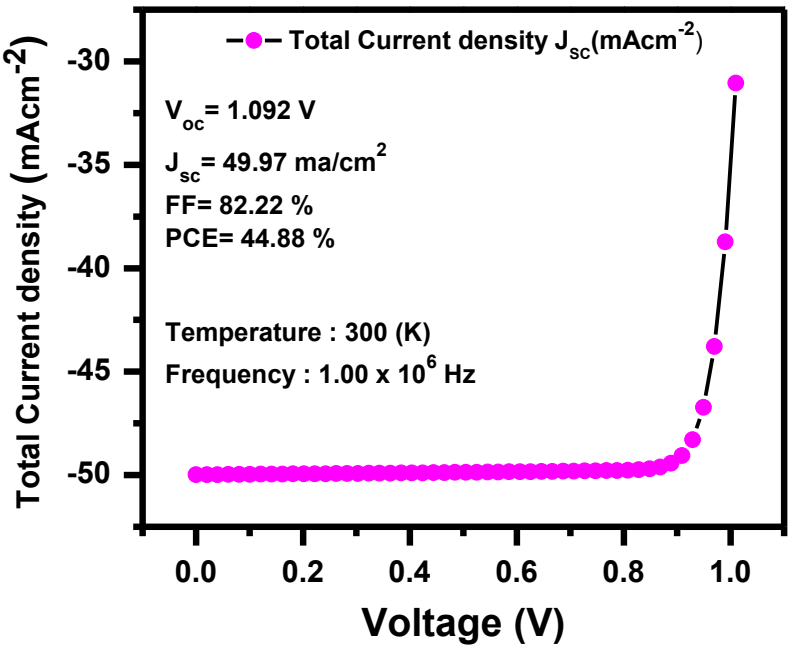


Figure-12. J-V Characteristics of (Au/Spiro-OmeTAD/Cs_2AgBiI_6 /CIGS /CdS /TiO_2) Solar cell.

The plot of quantum efficiency (QE) against wavelength is very significant for evaluating solar cell performance as shown in figure 13. It displays the percentage of absorbed photons of different wavelengths, revealing the capability of PV cell to convert different available wavelengths of sunlight into electrical output energy. QE peaks at specific wavelengths, corresponding to the most effective absorption of light inside the solar cell, which may be associated with the semiconductor material's E_g. A higher QE value indicates a more effective solar cell, signifying greater percentage of incoming photons getting absorbed and transformed into output. Figure 13 displays the QE trend across UV, visible and IR regions ranging from 300nm to over 1200 nm. While absorption is relatively low in the UV region, The highest absorption occurs within the visible region, specifically between 400 – 650 nm, with favorable absorption also observed in the near-infrared region. The maximum QE value corresponds to efficient sunlight absorption whereas the QE drops swiftly in far-infrared wavelength region, leading to diminished overall device output. This absorbed energy is then converted into electrical energy through various processes within the solar cell. Greater quantum efficiency results in improved performance output of the solar cells.

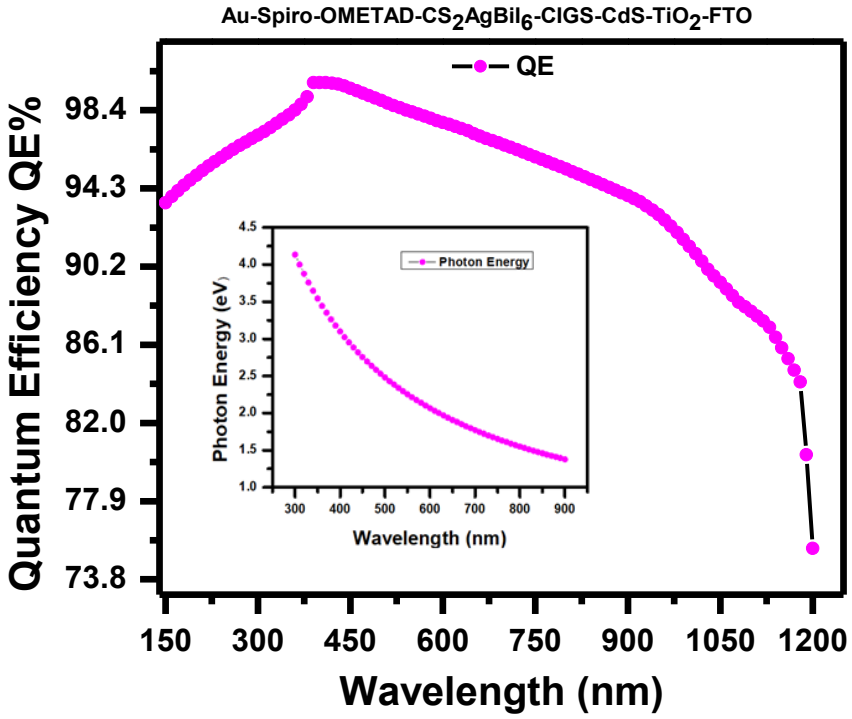


Figure-13. QE versus wavelength and photon energy versus wavelength in the inset.

Recombination is a major limiting factor in the performance of solar cells which reduces device output. Recombination occurs as the electrons and holes generated by sunlight come close to each other and vanish before reaching their relevant electrodes, resulting in energy loss and decreased output efficiency. Perovskite solar cells face various recombination mechanisms, including trap-assisted, bulk, and surface recombination, radiative and non-radiative. To improve performance, reducing recombination is crucial. Strategies may include passivation of interface defects and surfaces, optimizing perovskite layer thickness, and improving interlayer interfaces. Figure 14 shows how charge recombination varies with the diffusion length in the structural composition of perovskite solar cell. Initially, no recombination occurs up to a depth of 2.2 μm. Then a significant increase in carrier recombination occurs between 2.2 to 3.1 μm. Notably a constant trap-assisted recombination is observed throughout the entire diffusion length, peaking at 2.4×10^{20} $cm^{-3}s$ at 3.0 μm. The lower the recombination rate, the better the device performance.

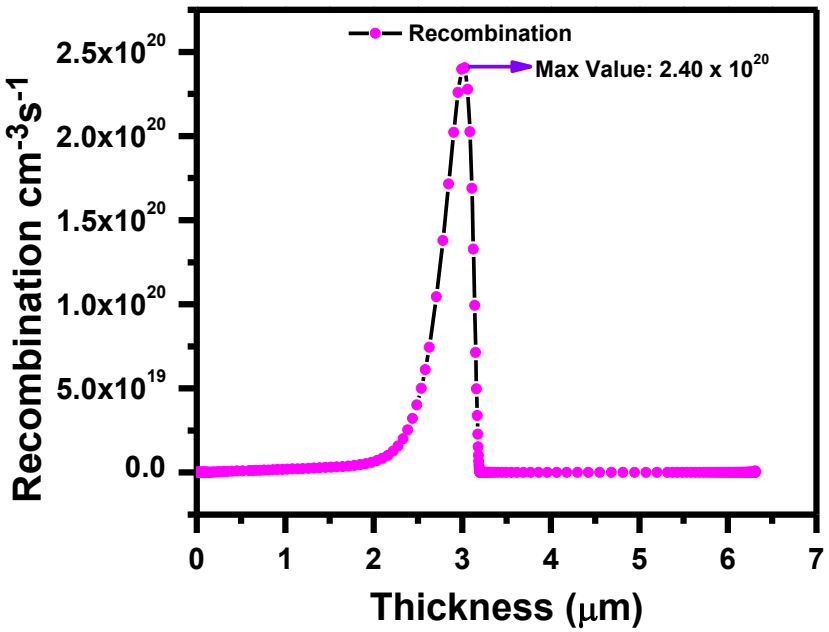


Figure-14. Surface depth versus recombination rate.

The process of generating charge carriers is crucial step in solar cell operation. When sunlight is absorbed by the solar cell material, it energizes the electrons, creating charge carriers that produce an electrical current. Therefore, the efficiency of PV cell depends on the rate of charge carrier generation. The optimization of this process is vital to increase solar cell efficiency, which is essential for widespread energy adoption through sunlight. The charge carrier generation rate is primarily determined by semiconductor material's absorption coefficient and intensity of the incident light. When sunlight hits a semiconductor material, photon energies equal to or greater than E_g of material may get absorbed, creating charge carriers in pairs. The absorption coefficient defines the probability of this absorption and depends on the material properties and incident light wavelength. Figure-15 shows how the charge carrier generation rate varies with depth within the solar cell composition, including the HTL, absorbers and ETL layers. Notably, no carrier generation occurs up to a thickness of 5.5 μm. However, from 5.5 μm to 6.4 μm, there is a substantial rise in carrier generation, peaking at 2.7 x 10^{22} $cm^{-3}s$ at the 6.4 μm. This understanding is crucial for optimizing solar cell efficiency. Through minor adjustments in integrated layers, the device output may be enhanced. It has been noticed that there is a significant difference between the values of carrier recombination as well as generation. The higher the generation rate relative to the recombination rate, the greater the device output.

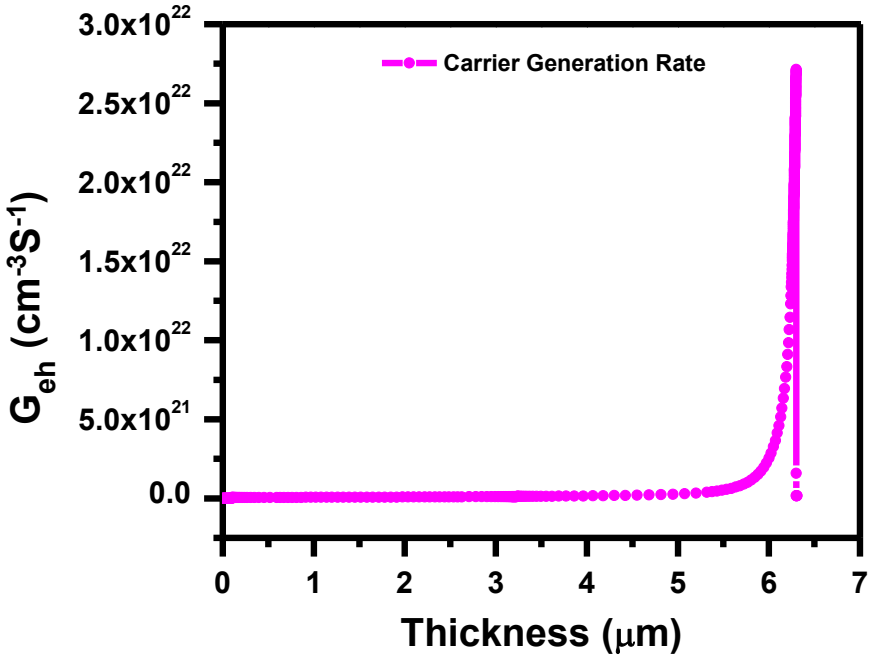


Figure-15. Generation rates of optimized solar cell.

Figure 16 illustrates the optimized energy band alignment for the Cs_2AgBiI_6-based PV cell, demonstrating a favorable configuration to achieve higher photovoltaic performance. Through the obtained fine-tuned value of Eg = 1.404 eV for Cs_2AgBiI_6, 1.50 eV for CIGS, 3.17 eV for Spiro-OMETAD, 2.44 eV for CdS and 3.2 eV for TiO_2, the optimal band gap alignment has been achieved. The lowest conduction band (CBL) and highest valence band (VBH) positions of each material determine charge carrier dynamics in the form of increased mobility. Higher mobility reduces charge recombination losses and facilitates efficient charge carrier transport. The well-aligned Fermi-level positions at the interfaces increase carrier separation and transport, reducing the recombination and improving the overall solar cell efficiency. The mobility of charge carriers significantly impacts device performance. Increasing electron and hole mobilities enhances the PCE of the overall device. Also, by engineering materials with high carrier mobility, optimizing interface properties, and minimizing defects, significant improvements in solar cell efficiency and stability may be achieved.

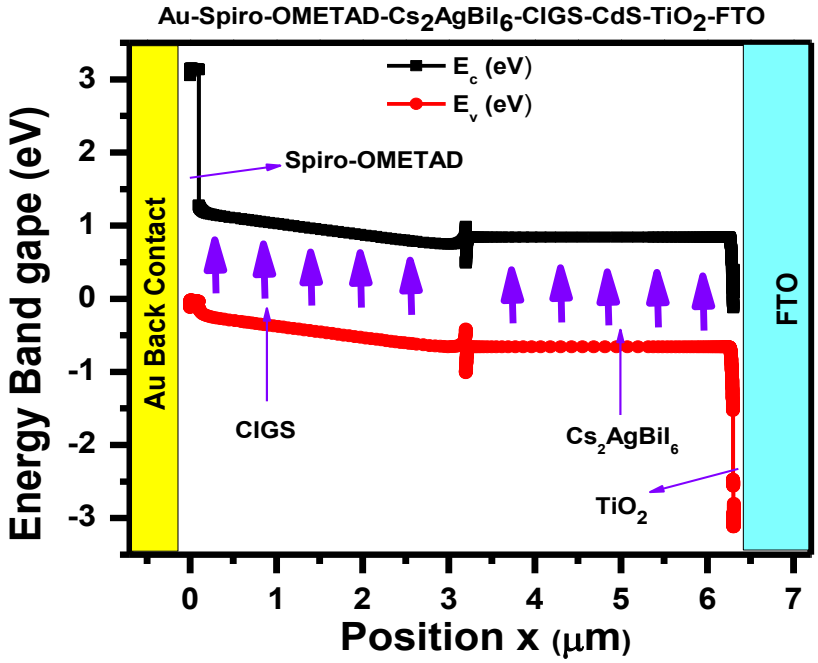


Figure-16. Optimized energy band diagram of solar cell.

6. Solar Cell Optimization

6.1 Effect of thickness variation of TiO_2 (ETL)

The TiO_2 -ETL plays an important role in perovskite solar cell performance by facilitating the collection and movement of electrons generated inside the perovskite absorber towards the outer circuit. Additionally, the electron transport layer (ETL) effectively blocks the backflow of holes from the HTL and reduces electron-hole recombination. It aids in aligning the conduction and valence band edges of the perovskite with those of the electrode for efficient carrier extraction, thereby enhancing V_{oc} and improving the overall PCE. The impact of TiO_2 (ETL) thickness variation on output parameters (V_{oc}, J_{sc}, FF and PCE) was then analyzed. The layer thickness was varied from 0.005 to 0.020 μm while maintaining constant Cs_2AgBiI_6, CIGS, and Spiro-OMeTAD layer thicknesses, it was observed that the device showed the highest PCE at optimized layer thickness. Figure 17 shows a thickness variation on electrical parameters.

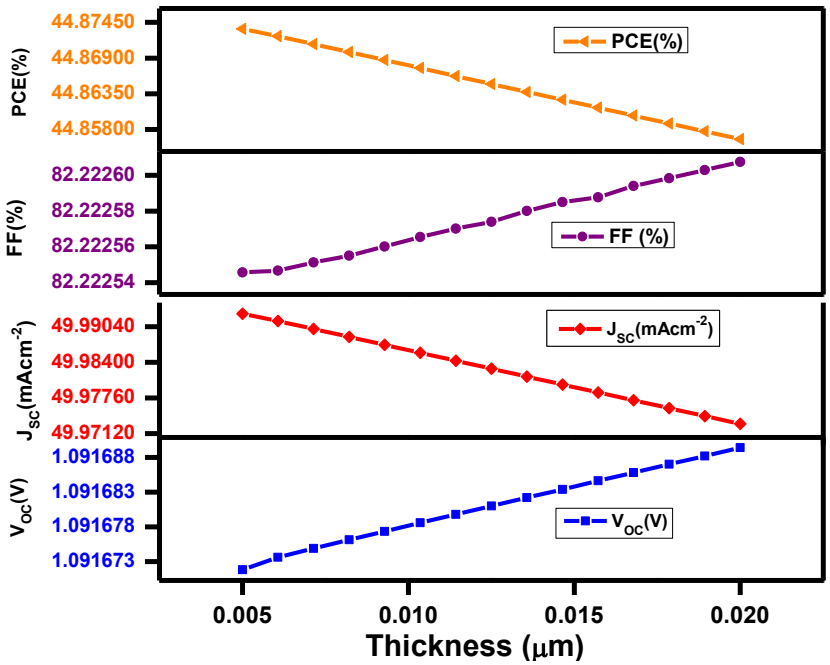


Figure-17. Electrical parameters versus thickness of TiO_2-ETL.

6.2 Effect of Cs_2AgBiI_6 Absorber Layer Thickness Variation

Figure 18 presents the impact of absorber layer thickness variation on the key electrical performance parameters (V_{oc}, J_{sc}, FF and PCE) of the Cs_2AgBiI_6 perovskite layer. Notably, the fill factor (FF) gradually increases with thickness and current density (J_{sc}) exhibits a decrease with increasing layer thickness, whereas the V_{oc} and PCE decrease beyond 2.9 μm. The optimal values for these parameters are achieved at a layer thickness of 3.1 μm, with V_{oc}, J_{sc}, FF and PCE reaching 1.095 V, 48.99 mA/cm^2, 82.186 % and 45.022% respectively.

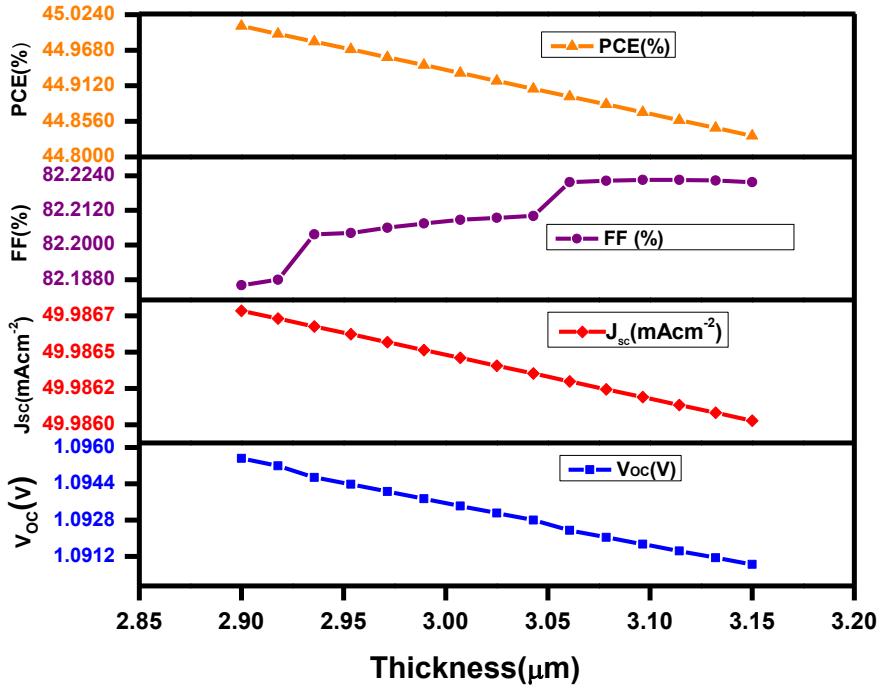


Figure-18. Electrical parameters versus thickness for Cs_2AgBiI_6 absorber

6.3 Effect of variation CIGS absorber layer thickness

Figure-19 illustrates the relationship between CIGS (absorber) thickness and electrical parameters. An increase in layer thickness results in a gradual rise in PCE, V_{oc}, and J_{sc}, whereas the fill factor exhibits minimal or inconsistent variation. A thicker absorber layer can potentially provide a greater number of charge carriers. The maximum recorded values for PCE, fill factor, J_{sc} and V_{oc} are, 44.40%, 82.20%, 49.50 mA/cm^2 and 1.05 eV, respectively, at an optimal CIGS absorber layer thickness of 3.1 μm. The observed decrease in fill factor (FF) with increasing absorber layer thickness can be attributed to the limited ability of photo-generated excitons to effectively traverse the increased thickness and overcome the internal barrier potential at the interfaces. Additionally, exposure to illumination intensity enhances carrier generation and mobility. However, exceeding ideal thickness values can lead to charge carrier recombination and reduced carrier lifetime in the CIGS layer.

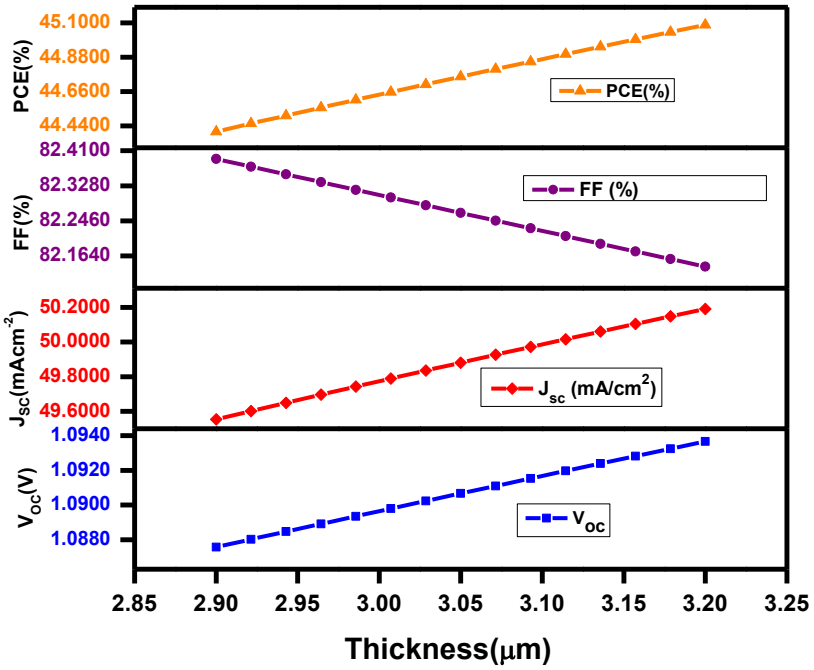


Figure-19. Electrical parameters versus thickness for CIGS.

6.4 Effect of Spiro-OMeTAD Thickness Variation

In solar cells, the hole transport layer (HTL) plays a crucial role in transporting holes generated by sunlight absorption inside the active absorber layer toward the electrode. Efficient hole transport and electron blocking by the HTL are essential for achieving high efficiency, as this mechanism prevents charge recombination and enhances overall device performance. Optimizing HTL performance can be achieved by adjusting its thickness, composition, and morphology. Thickness variation can impact device performance. Using SCAPS-1D, the impact of Spiro-OMeTAD thickness was investigated on perovskite solar cell performance, varying the thickness from 0.05 to 0.15 μm shown in figure 20.

The results revealed an optimized Spiro-OMeTAD thickness of 0.1μm, yielding the highest values of V_{oc}, J_{sc}, FF and PCE at 1.090V, 49.986 mA/cm^2, 82.221% and 44.86 %, respectively, indicating significant device performance improvement.

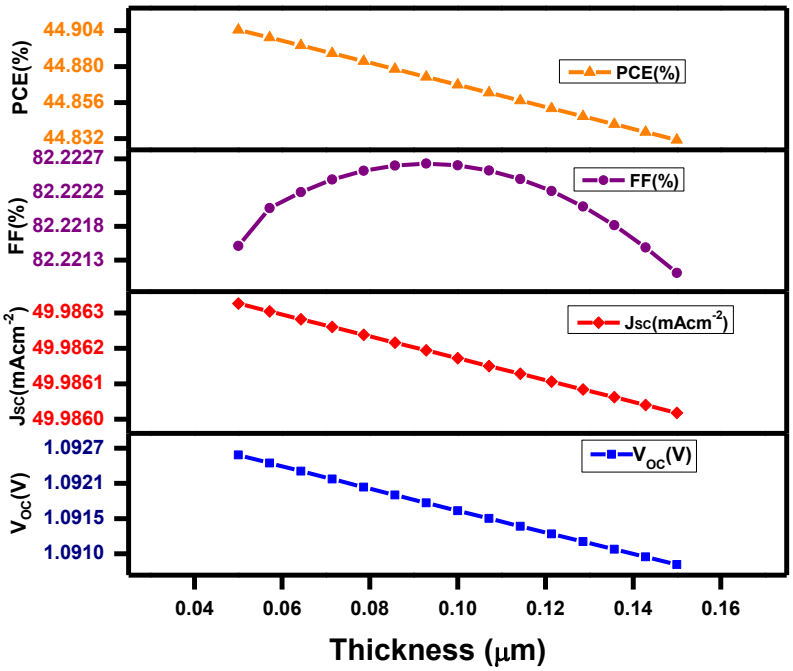


Figure-20. Electrical parameters versus thickness for Spiro-OMeTAD-HTL

6.5 Effect of variation of Temperature on solar cell Characteristics

Temperature has a significant impact on solar cell performance. The efficiency of the solar cell depends on how much energy it can get from the light that hits it, and temperature affects how well it can perform. At lower temperatures, photocarrier generation remains primarily determined by the incident photon flux and the optical absorption properties of the semiconductor. The temperature dependence of photovoltaic performance is governed by changes in band gap, carrier transport, recombination, and other device parameters. As it gets warmer, more charge carriers are made, the solar cell works better. However, if the temperature becomes too high, the solar cell performance suffers because charge carriers start colliding and getting lost, which reduces efficiency. Temperature is important when looking at how well solar cell works, because it affects the electrical properties, as shown in Figure 21. As temperature increases, the short circuit current density (J_{sc}) increases and reaches a peak value of 49.99 mA/cm^2 at 340 K. This is because more charge carriers are being made. Initially, FF decreases up to 317 K and then starts increasing. The temperature dependence of the short-circuit current density (J_{sc}) is influenced by changes in the semiconductor band gap, optical absorption, and carrier transport properties. The simulated variation in J_{sc} should therefore be interpreted in terms of the calculated optoelectronic and carrier-transport properties of the device. The temperature dependence of J_{sc} may arise from changes in the semiconductor band gap, optical absorption, carrier transport, and recombination processes, which helps the solar cell operate more efficiently.

The decrease in PCE with increasing temperature is mainly associated with the reduction in V_{oc}, together with temperature-dependent changes in the band gap, recombination, carrier transport, and resistive losses.

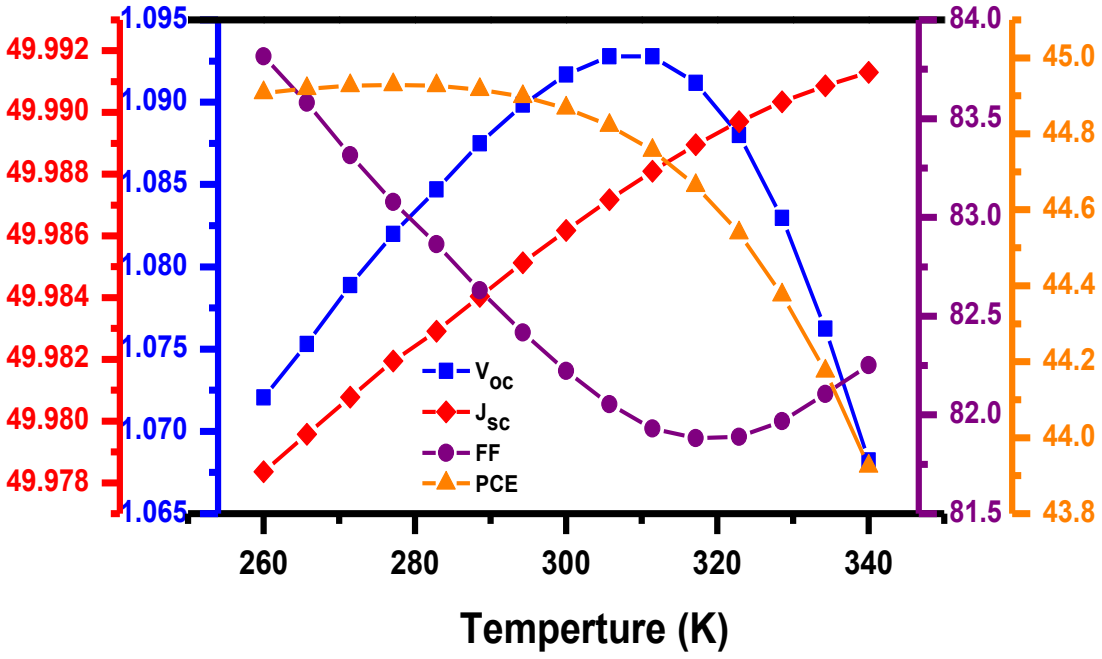


Figure-21. Electrical parameters with variation in temperature variation in temperature.

7. Solar Module Analysis

7.1 IV-Characteristics of solar module with variation of incident irradiation

After optimizing electrical parameters using a Solar Cell Capacitance Simulator in one dimension (SCAPS-1D), the results were verified through PVsyst, a solar cell and module design package. The optimized single-cell electrical parameters obtained from SCAPS-1D were used as input parameters for the PVSyst module simulation. The module-level results were then evaluated under different irradiance and temperature conditions. Theoretical calculations were performed to determine single-cell parameters, which served as input values for PVsyst module calculations consisting of 72 cells in series. Standard module dimensions (2.20 m × 1.10 m) and a weight of 30 kg were selected for the simulations. While many commercial solar modules have 72 or more cells there is a growing trend toward 144-cell panels

which are easier to install. The module performance was evaluated in PVSyst using the optimized electrical parameters obtained from the SCAPS-1D single-cell simulation under various solar irradiance levels was investigated as

shown in figure-22. The module dimensions were 2.20 m × 1.10 m, corresponding to an area of 2.42 m². At an irradiance of 1000 W/m², the incident solar power was 2420 W. The simulated maximum output power was 1025.9 W, corresponding to a module efficiency of approximately 42.4%. The voltage-current (IV) curves showed a strong increasing trend with illumination intensity from 200 W/m² to 1000 W/m² as shown in Figure 22. This increase in output current is primarily attributed to the enhanced generation of electron-hole pairs across all cells, thereby improving overall device performance. Output power rises proportionally with increasing irradiation intensity.

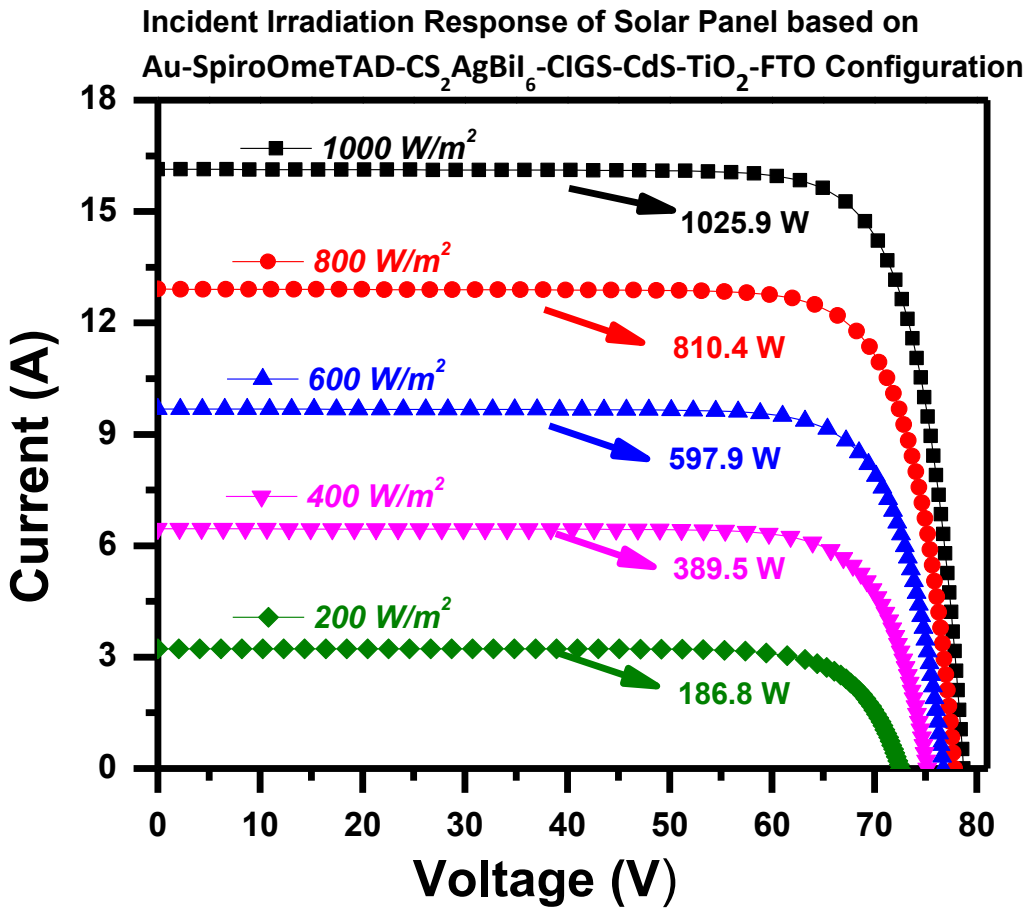


Figure 22. Characteristics of solar module at different incident irradiation.

7.2 IV-Characteristics of solar module with variation of temperature

The voltage versus current characteristics of solar module comprising 72 interconnected Au/Spiro-OMeTAD/Cs_2AgBiI_6/CIGS/CdS/TiO_2/FTO solar cells in series have been simulated in PVSyst software under standard solar irradiance of 1000 W/m², with temperature variations at 10°C, 26°C, 40°C, 66°C, and 70°C. The analysis shown in Figure 23 reveals significant influence of temperature on the power output (P_{max}), representing a typical temperature-dependent performance losses observed in photovoltaic (PV)

modules. The temperature-dependent performance of the proposed PV module was evaluated at different operating temperatures. The maximum power output decreased from 1054.4 W at 10°C to 1042.4 W at 25°C, 1030.1 W at 40°C, 1018.4 W at 55°C, and 1004.5 W at 70°C. This reduction is associated with the temperature dependence of the photovoltaic electrical parameters, particularly the open-circuit voltage.

losses at higher temperatures. The I-V curves indicate that while short-circuit current (I_{sc}) exhibits a marginal rise with rising temperature due to enhanced charge carrier generation, the decay in V_{oc} dominates, leading to an overall reduction in PCE.

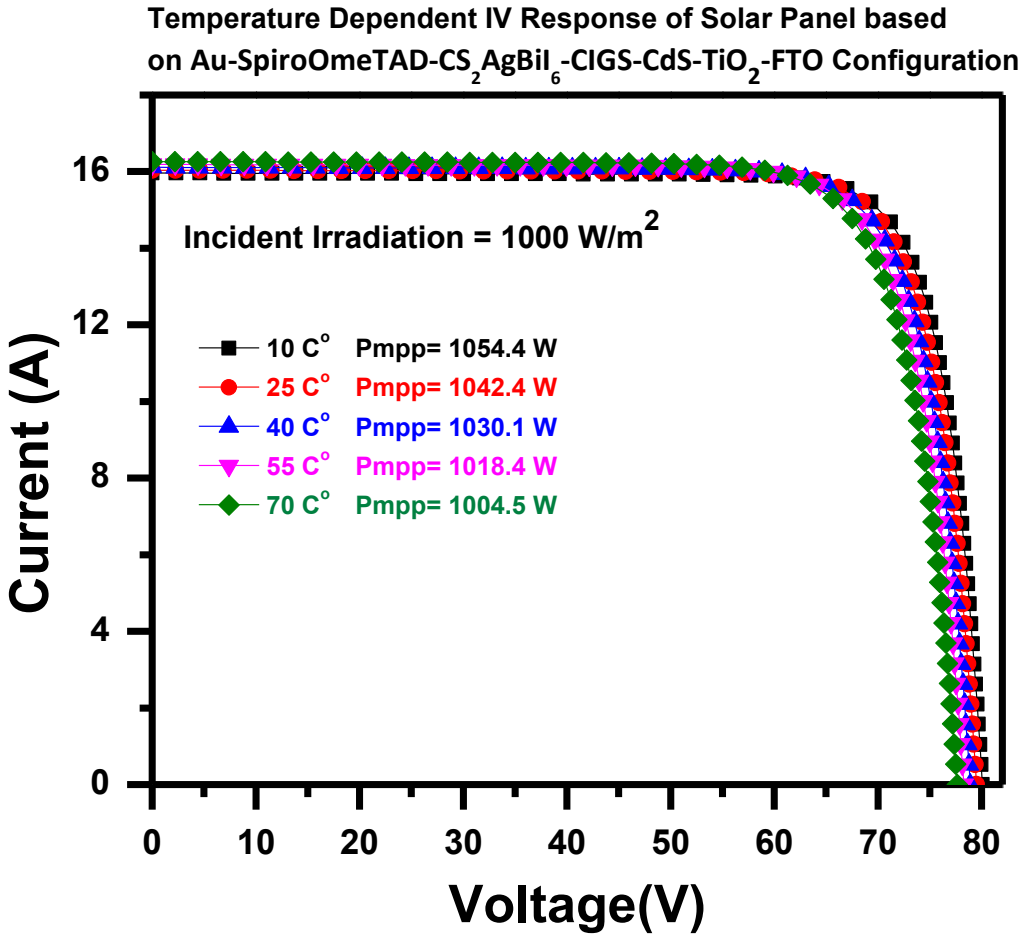


Figure-23. IV-Characteristics of solar module at different temperatures.

7.3 PV-Characteristics of solar module with variation of incident irradiation

Figure 24 shows the power output characteristics of the PV module. The results clearly demonstrate a direct relationship between incident radiation intensity and power output. With an increase in radiation intensity from 200 W/m² to 1000 W/m², the power output of the module also increases gradually. This connection is based on the fundamental principle of PV systems, where

higher sunlight intensity excites more electrons, generating more current within the semiconductor. The noted increase in the power output from 108.8W to 1025.9W across the tested incident radiation range highlights the panel's efficiency in converting sunlight into electrical energy. This enhancement plays a pivotal role in maximizing energy harvest, particularly in regions characterized by high solar irradiance levels. The steady increase in power output with each incremental rise in irradiance underscores the reliability and stability of the solar module's performance across diverse climatic conditions. A comprehensive understanding of the power output behavior under varying irradiance intensities is fundamental for precise energy yield forecasting and for the optimization of solar photovoltaic system design to achieve maximum operational efficiency.

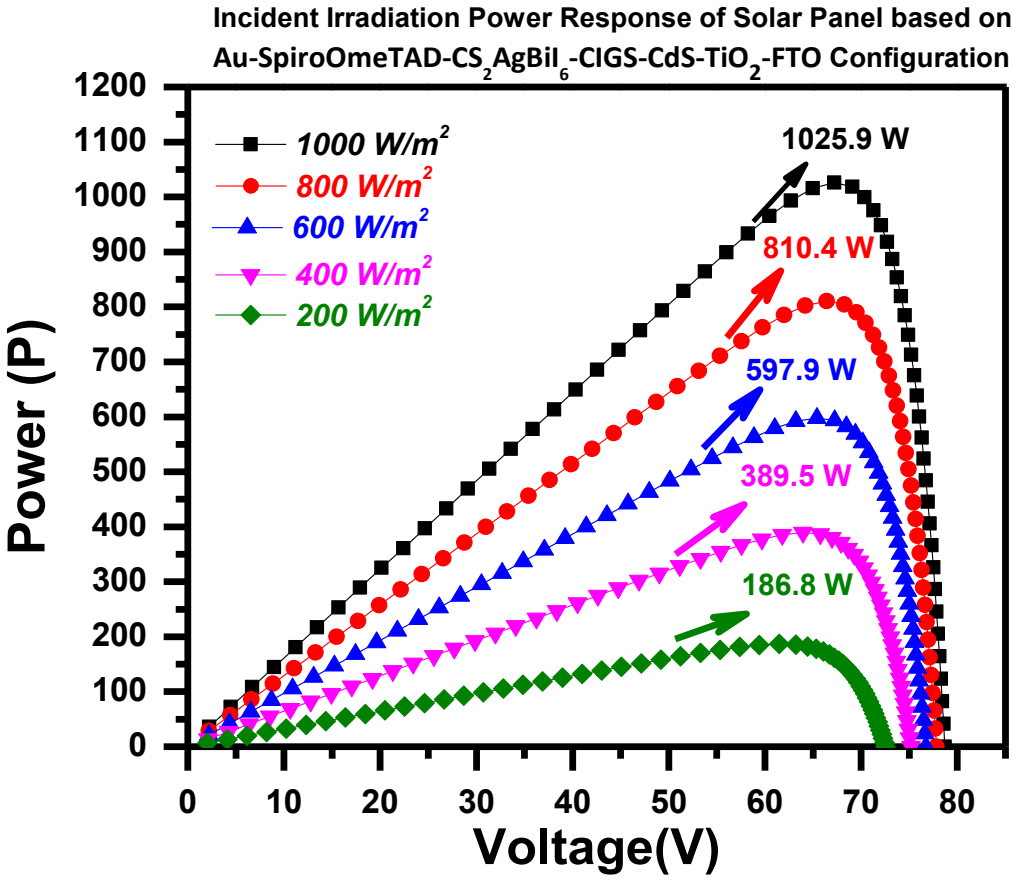


Figure-24 PV-Characteristics of solar module at different values of incident irradiation

7.4 PV-Characteristics of solar module at different values of temperature

The photovoltaic (PV) characteristics of a solar module comprising 72 interconnected Au/Spiro-OMeTAD/Cs_2AgBiI_6/CIGS/CdS/TiO_2/FTO solar cells were systematically analyzed using PVSyst software. The module was simulated for Islamabad, Pakistan, under the specified irradiance and

temperature conditions. The temperature-dependent performance of the module was assessed at a fixed irradiance of 1000 W/m², with simulations conducted over a temperature range of 10°C to 70°C. Five discrete operational temperature conditions were simulated, as depicted in figure-25, revealing a consistent deterioration in maximum power output (P_{max}) with rising temperature. The module delivered a maximum power of 1054.4 W at 10°C, which decreased to 1042.4 W at 25°C, 1030.1 W at 40°C, 1018.4 W at 55°C, and 1004.5 W at 70°C. This reduction in power conversion efficiency (PCE) is primarily attributed to temperature-dependent performance losses, including decreased charge carrier mobility, increased electron-hole recombination, and improved series resistance within the solar cells. I-V and P-V characteristics further confirm the increase in temperature generally reduces V_{oc}, while I_{sc} may increase slightly because of the temperature dependence of the band gap and carrier generation. The reduction in V_{oc} dominates the overall decrease in maximum, which collectively impact the total energy yield. Temperature dependent performance variations are critical for optimizing solar module efficiency, developing effective thermal management strategies, and confirming accurate energy output predictions under various environmental conditions.

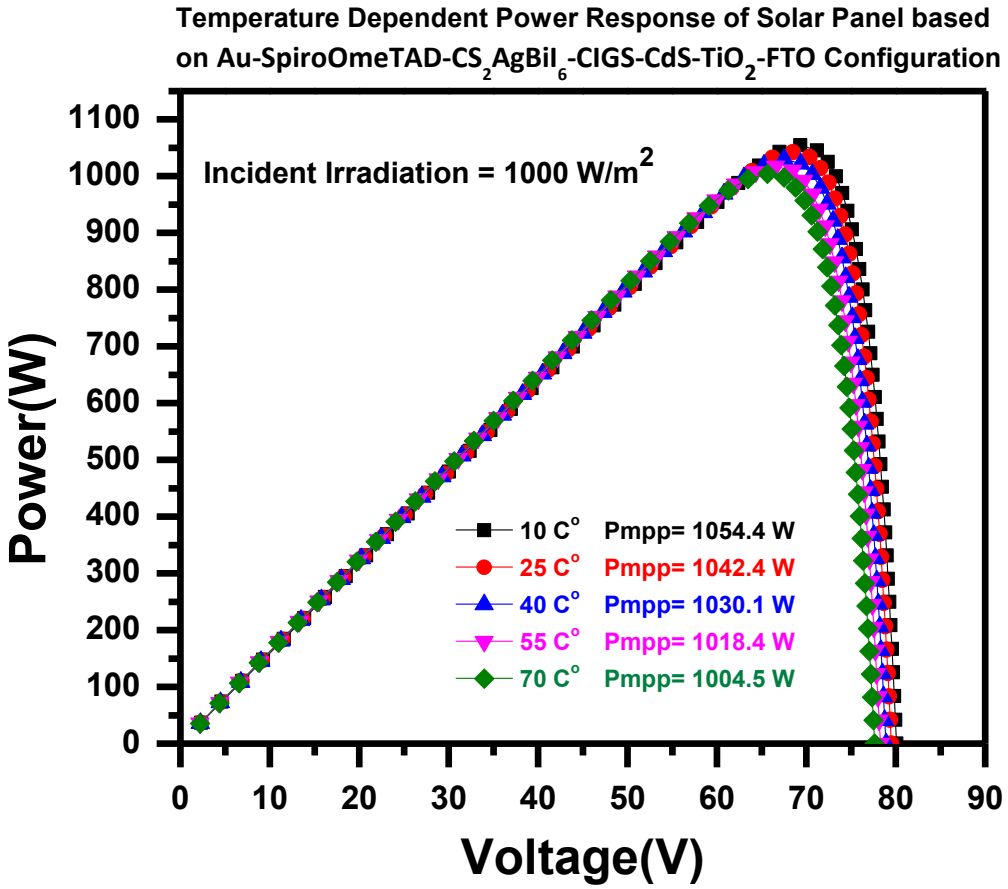


Figure-25 PV-Characteristics of solar module at different values of temperature

8. Conclusion

In this study, a novel Au/Spiro-OMeTAD/Cs_2AgBiI_6/CIGS/CdS/TiO_2/FTO solar cell architecture was meticulously designed and extended to an optimized high-performance solar module using SCAPS-1D and PVSyst simulations. The electrical parameters were significantly influenced by the optimized layer thicknesses of Cs_2AgBiI_6 (3.1 μm, absorber), CIGS (3.1 μm, secondary absorber), TiO_2 (0.01 μm, ETL), CdS (0.001 μm, buffer layer), and Spiro-OMeTAD (0.1 μm, HTL). The proposed structure achieved an outstanding power conversion efficiency (PCE) of 44.86%, with an open-circuit voltage (V_{oc}) of 1.092 V, short-circuit current density (J_{sc}) of 49.98 mA/cm^2, and a fill factor (FF) of 82.11%.

Interface defect densities in the proposed configuration affected charge carrier recombination, influencing the device output performance. The simulated device performance increased with diffusion length up to approximately 5.5 μm. The subsequent reduction in efficiency should be interpreted based on the specific parameter

dependencies and boundary conditions used in the simulation. The temperature-dependent output analysis revealed that optimal efficiency was attained between 260 K and 310 K, beyond which temperature-dependent performance losses such as increased recombination and decreased charge carrier mobility significantly impacted module performance. When scaled to a 72-cell module (dimensions: 2200 × 1100 mm), the proposed solar cell architecture delivered a power output of 1025.9 W under 1000 W/m^2 irradiation at room temperature, with a notable decline under reduced irradiation conditions when simulated in PVSyst. These findings establish the feasibility of the proposed lead-free, non-toxic, and greatly efficient solar cell and module design, offering a strategic corridor for next-generation photovoltaic technologies with enhanced sustainability and scalability.

Acknowledgements

The authors gratefully acknowledge the Electronics and Information Systems Department for providing access to SCAPS-1D software and thank Marc Burgelman of Ghent University for his assistance with the calculations and simulations

Funding

The authors received no funding for this work.

Declaration of Competing Interest

The authors assert that they possess no recognized conflicting financial interests or personal affiliations that might have seemingly affected the work presented in this study.

References

[1] A. Bala, and V. Kumar, Research gate, 00, 005400 (2021), DOI: 10.1103/PhysRevMaterials.00.005400.

[2] F. Ji, G. Boschloo, F. Wang, and F. Gao, Sol. RRL 2023, 7, 2201112, DOI: 10.1002/solr.202201112.

[3] Y. Liu, Y. Huang, Z. Yang, Y. Li, J. Xu, H. Li, W. Chen, * and K. Chen, ACS Appl. Energy Mater. 2023, 6, 5188−5196. DOI.org/10.1021/acsaem.3c00079 A.

[4] J. Dai, L. Ma, M. Ju, J. Huang, and X.C. Zeng, rsc.li/pccp. 21/07/2017, DOI: 10.1039/C7CP03448B.

[5] Z. Abdin, I. Qasim, M. Imran Malik, and M. Rashid, Heliyon 9 (2023) e14802, DOI.org/10.1016/j.heliyon. 2023.e14802.

[6] A. Bhorde, R. Waykar, Sachin R. Rondiya, S. Nair, G. Lonkar, A. Funde, Nelson Y. Dzade, and S. Jadkar. ES Mater. Manuf., 2021, 12, 43-52, DOI: https://dx.doi.org/10.30919/esmm5f1042.

[7] H. C. Sansom, G. Longo, A. D. Wright, L. R. V. Buizza, S. Mahesh, B. Wenger, M. Zanella, M. Abdi-Jalebi, M. J. Pitcher, M. S. Dyer, T. D. Manning, R. H. Friend, L. M. Herz, H. J. Snaith, J. B. Claridge, and M. J. Rosseinsky. J. Am. Chem. Soc. 2021, 143, 3983−3992, DOI.org/10.1021/jacs.1c00495.

[8] M. Awais Rehman, J. Rehman, and M. B. Tahir. Journal of Physics and Chemistry of Solids 181 (2023) 111443, DOI.org/10.1016/j.jpcs.2023.111443.

[9] A. Hajjiah, M. Gamal, I. Kandas, N. E. Gorji, and N. Shehata. Solar Energy Materials and Solar Cells 248 (2022) 112026 DOI.org/10.1016/j.solmat.2022.112026.

[10] P. Giannozzi, S. Baroni, N. Bonini, M. Calandra, R. Car, C. Cavazzoni, D. Ceresoli, G. L. Chiarotti, M. Cococcioni, I. Dabo, A. Dal Corso, S. Fabris, G. Fratesi, S. de Girandole, R. Gebauer, U. Gerstmann, C. Gougoussis, A. Kokalj, M. Lazzeri, L. Martin-Samos, N. Marzari, F. Mauri, R. Mazzarello, S. Paolini, A. Pasquarello, L. Paulatto, C. Sbraccia, S. Scandolo, G. Sclauzero, A.P. Seitsonen, A. Smogunov, P. Umari, and R.M. Wentzcovitch," J. Phys. Condens. Matter, vol. 21, no. 39, 2009, DOI: 10.1088/0953-8984/21/39/395502.

[11] S. Idrissi, H. Labrim, L. Bahmad, and A. Benyoussef. Chemical Physics Letters 766 (2021) 138347, DOI: org/10.1016/j.cplett.2021.138347.

[12] M. Shihab Uddin, M. Khalid Hossain, M. Borhan Uddin, G. F. I. Toki, M. Ouladsmane, Mirza H. K. Rubel, Daria I. Tishkevich, P. Sasikumar, R. Haldhar, and R. Pande. Adv. Electron. Mater. 2024, 2300751. DOI: 10.1002/aelm.202300751.

[13] Y. Naceur, H. Bourbaba, M.A. Ghebouli, L. Krache, B. Ghebouli, T. Chihi, M. Fatmi and S. Alomairy. Scientific Reports (2022) 12:8345 DOI: org/10.1038/s41598-022-12570-1

[14] M. Gajdoš, K. Hummer, and G. Kresse. PHYSICAL REVIEW B 73, 045112 2006. DOI: 10.1103/PhysRevB.73.045112

[15] K. Schwarz, P. Blaha, G.K.H. Madsen Electronic structure calculations of solids using the WIEN2k package for material sciences Comput Phys Commun, 147 (2002), pp. 71-76. https://doi.org/10.1016/S0010-4655(02)00206-0

[16] B. Shabbir, M. Nadeem, Z. Dai, M. S. Fuhrer, Q. K. Xue, X. Wang, and Q. Bao, Applied Physics Reviews, Vol. 5, 041105 (2018). 10.1063/1.5040694

[17] Babar Shabbir, Jingying Liu,Vaishnavi Krishnamurthi, R. A. W. Ayyubi, Kevin Tran, Sherif Abdulkader Tawfik, M. Mosarof Hossain, Hareem Khan,Yingjie Wu, Bannur Nanjunda Shivananju, Rizwan Ur Rehman Sagar, Asif Mahmood, Adnan Younis, Md Hemayet Uddin, Syed A. Bukhari, Sumeet Walia, Yongxiang Li, Michelle J.S. Spencer, Nasir Mahmood and Jacek J. Jasieniak, Advanced Functional Materials, Volume 32, Issue 3, Special Issue: Focus Issue on the Australian National Fabrication Facility, January 14, 2022, 2105038, https://doi.org/10.1002/adfm.202105038

[18] V. Krishnamurthi, H. Khan, T. Ahmed, A. Zavabeti, S. A. Tawfik, S. K. Jain, M. Spencer, S. Balendhran, K. B. Crozier, Z. Li, L.Fu, M. Mohiuddin, M. X. Low, B. Shabbir, A. Boes, A. Mitchell, C. F. McConville, Y. Li, K. K. Zadeh, N. Mahmood and S. Walia, Advanced Materials, Vol. 32, 45, 2004247 (2020).DOI: 10.1002/adma.202004247

[19] F. Tran, P. Blaha Accurate band gaps of semiconductors and insulators with a semilocal exchange-correlation potential Phys Rev Lett, 102 (22) (2009), pp. 226401-226404. https://doi.org/10.1103/PhysRevLett.102.226401
[20] S. Jiang, Y. Fang, R. Li, H. Xiao, J. Crowley, C. Wang, et al. Pressure-dependent polymorphism and band gap tuning of methyl ammonium lead iodide perovskites Angew Chem Int Ed, 55 (2016), p. 6540.https://doi.org/10.1002/anie.201601788
[21] G.K.H. Madsen, D.J. Singh, P. BoltzTra A code for calculating band-structure dependent quantities Comput Phys Commun, 175 (2006), pp. 67-71. https://doi.org/10.48550/arXiv.cond-mat/0602203
[22] Huang, L., Sun, X., Li, C., Xu, R., Xu, J., Du, Y. & Zhang, J. (2016). Electron transport layer-free planar perovskite solar cells: further performance enhancement perspective from device simulation. Solar Energy Materials and Solar Cells, 157, 1038-1047. https://doi.org/10.1016/j.solmat.2016.08.025
[23] B. Shabbir, M. Nadeem, Z. Dai, M. S. Fuhrer, Q. K. Xue, X. Wang, and Q. Bao, Applied Physics Reviews, Vol. 5, 041105 (2018). 10.1063/1.5040694.
[24] Owais Ahmad, Irfan Qasim, Syed M. Hasnain, Zain ul Abdin, Muhammad Farooq Nasir, Muhammad Imran Malik, Asim Rashid, "Modelling and numerical simulations of eco-friendly double absorber solar cell "Spiro-OmeTAD/CIGS/$MASnI_3$/CdS/ZnO" and its PV-module"Organic Electronics 117 (2023) 106781, https://doi.org/10.1016/j.orgel.2023.106781
[25] Chowdhury, M. S., Shahahmadi, S. A., Chelvanathan, P., Tiong, S. K., Amin, N., Techato, K. A., & Suklueng, M. (2020). Effect of deep-level defect density of the absorber layer and n/i interface in perovskite solar cells by SCAPS-1D. Results in Physics, 16, 102839. https://doi.org/10.1016/j.rinp.2019.102839
[26] I. Qasim, and M. I. Malik, Energy Technol. 2023, 11, 2300471, https://doi.org/10.1002/ente.202300471.
[27] A. Khalid, M. I. Malik, and I. Qasim, Chem. Inorg. Mater. 2025, 5, 100083, https://doi.org/10.1016/j.cinorg.2024.100083
[28] Izadi, F., Ghobadi, A., Gharaati, A., Minbashi, M., & Hajjiah, A. (2021). Effect of interface defects on high efficient perovskite solar cells. Optik, 227, 166061. https://doi.org/10.1016/j.ijleo.2020.166061
[29] Jamal, M. S., Shahahmadi, S. A., Wadi, M. A. A., Chelvanathan, P., Asim, N., Misran, H., & Akhtaruzzaman, M. (2019). Effect of defect density and energy level mismatch on the performance of perovskite solar cells by numerical simulation. Optik, 182, 1204-1210. https://doi.org/10.1016/j.ijleo.2018.12.163
[30] Mandadapu, Usha, et al. "Design and simulation of high efficiency tin halide perovskite solar cell." Int. J. Renew. Energy Res 7.4 (2017). https://doi.org/10.20508/ijrer.v7i4.6182.g7270
[31] Gan, Y., Bi, X., Liu, Y., Qin, B., Li, Q., Jiang, Q., & Mo, P. (2020). Numerical investigation energy conversion performance of tin-based perovskite solar cells using cell capacitance simulator. Energies, 13(22), 5907. https://doi.org/10.3390/en13225907
[32] Jayan, K. D., & Sebastian, V. (2021). Comprehensive device modelling and performance analysis of $MASnI_3$ based perovskite solar cells with diverse ETM, HTM and back metal contacts. Solar Energy, 217, 40-48. http://dx.doi.org/10.1016/j.solener.2021.01.058
[33] Zhang, H., Ji, X., Yao, H., Fan, Q., Yu, B., & Li, J. (2022). Review on efficiency improvement effort of perovskite solar cell. Solar Energy, 233, 421-434. https://doi.org/10.1016/j.solener.2022.01.060
[34] H. Absike, N. Baaalla, R. Lamouri, H. Labrim, and H. Ez-zahraouy. Int J Energy Res. 2022; 46:11053–11064. DOI: 10.1002/er.7907

Supplementary Files

This is a list of supplementary files associated with this preprint. Click to download.

- GraphicalAbstract.docx